OPTICALLY TRANSPARENT METAMATERIAL RF ABSORBERS

A THESIS SUBMITTED TO

THE GRADUATE SCHOOL OF ENGINEERING AND SCIENCE

OF BILKENT UNIVERSITY

IN PARTIAL FULFILLMENT OF THE REQUIREMENTS FOR

THE DEGREE OF

MASTER OF SCIENCE

IN

ELECTRICAL AND ELECTRONICS ENGINEERING

By

Furkan Şahin

May 2023

OPTICALLY TRANSPARENT METAMATERIAL RF ABSORBERS

By Furkan Şahin

May 2023

We certify that we have read this thesis and that in our opinion it is fully adequate, in scope and in quality, as a thesis for the degree of Master of Science.

Vakur Behçet Ertürk(Advisor)

Hilmi Volkan Demir(Co-Advisor)

Ayhan Altıntaş

Birsen Saka Tanatar

Approved for the Graduate School of Engineering and Science:

Orhan Arıkan
Director of the Graduate School

ABSTRACT

OPTICALLY TRANSPARENT METAMATERIAL RF ABSORBERS

Furkan Şahin
M.S. in Electrical and Electronics Engineering
Advisor: Vakur Behçet Ertürk
Co-Advisor: Hilmi Volkan Demir
May 2023

Recent advances in metamaterials have allowed to impart unique properties to flat RF absorbers including broadband absorption, low thickness (in terms of the longest operating wavelength) and polarization insensitiveness, all essential to high-performance absorbers. For these RF absorbers, introducing additional properties of high optical transparency (in the visible range) and mechanical robustness opens up also stealth window applications. However, achieving all of these critical characteristics in a single design is a challenging task. In this thesis, to address this challenge, we propose and demonstrate an optically transparent, broadband, and polarization-insensitive RF absorbing metamaterial that is extremely thin (thickness = $0.079\lambda_L$; λ_L: longest operating wavelength). Our design consists of a single dielectric layer of polymethyl methacrylate (PMMA) sandwiched between the top and bottom indium tin oxide (ITO) films, altogether providing high optical transmission. The bottom ITO film acts as a ground plane, which reduces the RF transmission significantly. On the other hand, the top ITO film adorns a unique pattern that minimizes the RF reflection across a particular frequency range. Here we obtained these customized ITO patterns using a novel design methodology. We developed the fabrication process specific to the proposed RF structure and fabricated their prototypes. To validate numerical simulation results, we measured experimentally the RF absorption of these fabricated prototypes. The experimental results show that the proof-of-concept absorbers achieve over 90% absorption between 4.4-11.2 GHz and over 95% absorption between 4.8-10.6 GHz. Furthermore, we found the fabricated absorbers to be insensitive to polarization angles and preserve 90% absorption for oblique incidence angles of 60° for TM and 40° for TE polarizations in agreement with the numerical predictions. Also, besides RF characterizations, we optically recorded the transmittance in the visible range to be 65% on average for the tested absorbers.

These findings indicate that the proposed single-dielectric-layered architecture of optically transparent, broadband, polarization-insensitive RF absorbers, featuring a record relative thickness of $0.079\lambda_L$, holds great promise for use in stealth window applications.

Keywords: Metamaterials, RF absorbers, optically transparency, broadband absorption, polarization insensitivity.

ÖZET

OPTİK GEÇİRGENLİĞİ YÜKSEK MİKRODALGA METAMALZEME TABANLI SOĞURUCULAR

Furkan Şahin
Elektrik ve Elektronik Mühendisliği, Yüksek Lisans
Tez Danışmanı: Vakur Behçet Ertürk
Tez Eş-Danışmanı: Hilmi Volkan Demir
Mayıs 2023

Metamalzeme alanındaki yenilikler, düz mikrodalga soğuruculara geniş bantta soğurma, düşük kalınlık (çalışma frekansı bandındaki en büyük dalga boyu cinsinden) ve polarizasyondan bağımsızlık gibi yüksek performanslı mikrodalga soğurucular için zaruri olan özgün özellikler sağlamıştır. İlaveten, mikrodalga soğurucular için görünür bölgede yüksek optik geçirgenlik ve mekanik dayanıklılık gibi ek özellikler kazandırmak radar izi düşük pencere uygulamalarının önünü açmıştır. Ancak tüm bu kritik özelliklere tek bir tasarımda ulaşmak oldukça zordur. Bu tezde, bu zorluğu adreslemek üzere, optik geçirgenliği yüksek, geniş bantta ve polarizasyon açısından bağımsız, metamalzeme tabanlı çok ince (kalınlık = 0.079 λ_L; λ_L: en yüksek çalışan dalgaboyu) bir mikrodalga soğurucu önerilmiş, tasarlanmış ve ölçümlerle doğrulanmıştır. Tasarım, tamamı yüksek optik geçirgenlik sağlayan alt ve üst katman indium tin oxide (ITO) filmlerinin arasına sıkıştırılmış bir polymethyl methacrylate (PMMA) dielektrik katmanından oluşmaktadır. Alt ITO katmanı bir topraklama yüzeyi olarak davranmakta ve mikrodalga geçirgenliği yüksek oranda azaltmaktadır. Diğer taraftan, üst ITO filmi sahip olduğu özgün şekiller sayesinde belirli bir frekans bandı için mikrodalga yansımalarını mümkün olduğu kadar düşürmektedir. Bu ITO şekilleri özgün bir tasarım metodolojisi ile elde edilmiştir. Bu mikrodalga soğurucu tasarımlarına özgü bir üretim süreci geliştirilmiş ve prototipler üretilmiştir. Üretilen prototipin mikrodalga soğurma performansı deneysel olarak ölçülmüş ve simülasyonlar ile karşılaştırılmıştır. Deneysel sonuçlar, tasarlanan soğurucunun %90 ve üzeri soğurma değerlerini 4.4-11.2 GHz bandında ve %95 ve üzeri soğurma değerlerini 4.8-10.6 GHz aralığında sağladığını göstermektedir. Ayrıca, üretilen soğurucunun polarizasyon açısından bağımsız olduğu ve sayısal tahminleri doğrular nitelikte, %90 ve üzeri soğurma değerlerini 60°'ye kadar

TM ve 40°'ye kadar TE polarizasyonları için koruduğu görülmüştür. Mikrodalga karakterizasyonu yanında görünür bölgedeki optik geçirgenliğin, test edilen soğurucular için ortalama %65 olduğu ölçülmüştür. Tüm bunlar, önerilen tek katman dielektrikten oluşan, optik geçirgenliği yüksek, geniş bant ve polarizasyon bağımsız mikrodalga soğurucuların sahip oldukları 0.079 λ_L rekor oransal kalınlık değeriyle radar izi düşük pencere uygulamalarında kullanılmak üzere mükemmel bir aday olabileceğini ortaya koymaktadır.

Anahtar sözcükler: Metamalzemeler, mikrodalga soğurucular, optik geçirgenlik, geniş bant soğurma, polarizasyon bağımsızlığı.

Acknowledgement

First, I would like to express my deepest appreciation to my advisor, Prof. Vakur Behçet Ertürk. He has been a great role model for me and his guidance carried me through all of the stages in this study. I would also like to thank my co-advisor, Prof. Hilmi Volkan Demir, who accepted me for this position and supported me endlessly. His scientific eagerness and vision are beyond the words. All in all, working with them was an inspiring experience for me and I could not have imagined better advisors for this thesis and project.

I would like to express my sincere gratitude to Emre Ünal, who contributed insightful comments and suggestions to this thesis. His great experience and immense knowledge in engineering made everything possible. I am also grateful to Özgün Akyüz for his unwavering support in terms of non-technical issues. Furthermore, I would like to thank the RF group members of Demir Research Group, Anıl Ç. Atak and Tuğba K. Kılıç. I could not have undertaken this journey without their great friendship and support. I am also thankful to other members of Demir Research Group for a great time spent together.

I would like to thank and acknowledge TUBITAK-BIDEB 2210-A Scholarship Program for the financial support of my MSc studies.

This endeavor would not have been possible without my family, my mother Sevgi, my father Mehmet, and my sister Bahar. I always felt their support and motivation.

Finally, my very special thanks and deepest gratitude go to İrem Sayın. Her understanding, sacrifices, and continuing support was invaluable. She was always by my side when times I needed help and encouragement. It would be impossible to complete my studies without her.

Contents

List of Figures

List of Tables

Chapter 1

Introduction

Metamaterials are human-made structures that change the electromagnetic properties of materials to acquire a variety of specific responses, for example, significantly improved electromagnetic absorption over a wide frequency range while being flat and thin [1]. Regarding the electromagnetic absorption, by designing the structural parameters of metamaterials, electromagnetic waves can be coupled within the design itself to achieve high absorption levels for a desired frequency band [2]. Furthermore, the recent advances in metamaterials allowed absorbers to have unique properties such as broadband absorption, small thickness-to-bandwidth ratio, and polarization insensitiveness.

Generally, the designs consist of top, middle, and bottom layers corresponding to a semi-conductive pattern, dielectric spacer, and continuous conductive layer. The bottom layer blocks all the electromagnetic fields, so it minimizes the transmission. The dielectric layer creates loss to the incoming waves. The top layer is responsible for the impedance matching to the air. The impedance matching theory suggests that the top layer provides an electric response to tune the relative permittivity ϵ_r. Furthermore, the relative permeability μ_r is tuned by the magnetic response, which is created by a combination of the top layer and the ground plane. When a metamaterial absorber satisfies the criterion of $\sqrt{\mu_r(\omega)\epsilon_r(\omega)} = Z(\omega) = 1$, which represents the normalized impedance of the absorber to the free space: when the effective impedance of the design matches with that of the free space, minimum reflection is achieved [3].

In literature, several theoretical models such as effective medium theory, transmission line modeling, coupled mode theory, and interference theory have been proposed to understand the absorption behavior [4]. In particular, the interference theory provides a simple mathematical model in comparison with the other models [5]. This model assumes two interfaces as the air-dielectric and dielectric-ground plane. When the air-dielectric interface is illuminated by a plane wave, partial reflection to the air and transmission of the remaining wave to the dielectric take place. During the propagation of transmitted wave, dielectric loss is effective and perfect reflection is assumed off the ground plane. This totally reflected wave experiences further reflections and transmissions from the top layer. At the end, the wave undergoes multiple reflections and transmissions between the two interfaces. The overall reflection can be calculated by a formula that uses the superposition of multiple reflections [6]. Then, the absorption can be retrieved from the reflection as follows:

$$A(\omega) = 1 - R(\omega) = 1 - |S_{11}|^2 \tag{1.1}$$

where A(ω) stands for the absorption and R(ω) represents the reflection. The S_{11} term contains both co-polarization and cross-polarization components, and $|S_{12}|^2$ term is not included due to the assumption of perfect reflection off the ground plane.

Apart from the high absorption in a wide band, metamaterial absorbers can possess an ultra-thin thickness, polarization insensitiveness, wide oblique incidence angle tolerance and light weight. Owing to these properties, they have been extensively used in microwave applications including reconfigurable sensing, energy harvesting, absorbing undesired signals for stealth purposes, and EMI/EMC applications in different industries, including security, military, medical, and astronomy [7]-[11]. On the other hand, most of the designs used in these areas typically provide no optical transparency in the visible. The lack of optical transparency decreases the number of possible applications for stealth aircraft windows and radio frequency identification (RFID) systems [12].

However, in recent years, metamaterial absorbers with optically transparent characteristics have been investigated. In the fabrication process, graphene, indium tin oxide (ITO), or other conducting oxides are used as the transparent conductive films [13]. Furthermore, transparent dielectric spacers are chosen in the designs. As a result of these improvements, optically transparent metamaterial absorber applications have emerged in many areas such as microwave invisible solar panels, curved-surface RF absorbers, stealth windows of electromagnetically shielded buildings and low-IR microwave transparent absorbers [14]-[17].

As can be understood from the aforementioned applications, metamaterial absorbers provide a high absorption across a wide bandwidth. However, minimizing the thickness and achieving polarization insensitivity together with wide-angle stability for the same design has been a pending problem and extensive research to find appropriate designs that possess these features was conducted [18]. The broadband nature of the absorbers with the minimized thickness was studied using several different techniques including employing multilayer structures [19], [20] and multiple scaled versions of the same geometry within the unit cell [21], [22], introducing lumped elements [23], [24], and combining multi-resonant structures [25]-[27].

The multilayer structures suffer from practical problems such as difficulties in the alignment of layers even if they provide absorption in a wide band. To eliminate the need for multiple layers, the scaled versions of the same geometry within the unit cell was proposed. Nevertheless, this increases the cell dimensions and the fabrication complexity. Then, lumped elements were introduced to different unit cell types, which resulted in a single unit cell for the whole structure. However, soldering lumped elements adds another fabrication complexity. To eliminate this fabrication difficulty, multi-resonant structures that have complex geometries for a single unit cell were investigated. The geometries of these unit cells can be scaled versions of the same geometry or different geometrical shapes placed in a nested fashion. As a result, fabrication complexity is reduced significantly and high absorption with a low thickness is achieved for a single-type unit cell.

Circuit analog absorbers (CAA) can be considered as multi-resonant structures. These absorbers have a complex unit cell geometry that combines resistive sheets with reactive components. Thus, resistive sheets are replaced by lossy frequency selective surface (FSS) sheets that have complex sheet admittance, which enhances bandwidth [28]. Reactive parts of the complex sheet admittance are obtained from FSS unit cells that consist of straight parts and gaps (between the straight parts), which yield inductive and capacitive effects, respectively. Square loop arrays, crossed dipoles, or double-split serration ring type unit cells have been previously proposed in the literature [29]-[31]. Additionally, geometry tailoring or pixelation of geometrical shapes of unit cells were introduced [32]. By doing so, binary versions of patterns were created and different shapes were optimized with various algorithms.

On the other hand, robust response for different polarization and oblique incidence angles requires further design improvements. In literature, a complete symmetry of a metamaterial unit cell is preserved to make absorption polarization-insensitive [33], [34]. For wide-angle stability of the designs, some methods were reported to increase the oblique incidence response, for instance, introducing compensation layers [35], [36].

In this thesis, we proposed and demonstrated an optically transparent and extremely thin (thickness = 0.079 λ_L, λ_L: the largest operating wavelength) metamaterial absorber. This design is a multi-resonant structure that is made of a single layer of polymethyl methacrylate (PMMA) as the dielectric layer and ITO films as the top and bottom conducting layers. The bottom ITO layer has no patterns; thus, it acts as a ground plane at RF. On the other hand, the top ITO layer has a unique pattern optimized with a novel design methodology to minimize the reflections for all polarizations and oblique incidence angles.

A single square loop unit cell was considered as the initial design. However, a single square loop is generally used for narrow-band absorber designs. Then, we introduced 4 square loops inside a single unit cell and connected them with strips. By adopting this idea, a wideband absorption response was achieved. Furthermore, the unit cell exhibits horizontal, vertical, and diagonal symmetries that ensure the polarization insensitivity is accomplished.

Owing to the unit cell's symmetric nature, one unit cell was separated into 8 regions and we applied optimization only for one region. The optimization assumes that the unit cell consists of pixels that can have either a value of 1 or 0. These pixel values form a matrix that corresponds to the presence of ITO bricks in specific locations. The pixel matrix was fed into particle swarm optimization (PSO) and more than 90% absorption between 4.4 and 11.2 GHz as well as more than 95% absorption between 4.8 and 10.6 GHz were achieved. Due to the four-fold symmetry of this design, polarization insensitiveness is also preserved. Furthermore, simulations present that this design provides more than 90% absorption for incident angles up to 60° for TM and 40° for TE polarizations.

To assess the true performance of the designed absorber, a prototype was fabricated by combining ITO films with PMMA. The pattern of the top layer's ITO film was fabricated by a laser etching process. The prototype was characterized by a home-made measurement setup, which consists of antennas, a rotational stage, and holders. Furthermore, the antennas used in this setup were chosen as Vivaldi, horn, and double ridge horn type antennas owing to their attractive properties such as directive characteristics, wide operating bandwidth, and ease of construction. Initial measurements were performed using Vivaldi antennas thanks to their ease of design and fabrication. However, Vivaldi antennas presented some alignment problems during the measurements. Thus, horn antennas were considered next because of their mechanical stability, and X-band pyramidal horn antenna was fabricated, given its small size and fairly easy design. Nevertheless, the fabricated horn antenna could not achieve the extensive bandwidth that is required for the absorber measurement. As a result, last we fabricated a double ridge antenna with extensive bandwidth to be used in the measurement setup and measured the absorption of fabricated prototype under different oblique and polarization angles. The results matched fairly well with the simulations. Lastly, a 65% average optical transmittance in the visible wavelengths was measured using a spectrophotometer for the fabricated absorber. Both experimental and numerical findings indicate that the fabricated prototype of the proposed multi-resonant single-layer optically transparent metamaterial absorber can find use in stealth window applications because of its wide absorption bandwidth, stable performance for oblique and polarization angles, and high optical transmittance with mechanical robustness.

The organization of the thesis is as follows. Chapter 2 starts with the design of an optically transparent metamaterial absorber. Then, the unique design algorithm and simulations for this absorber are provided. Last, the fabrication process is presented. Chapter 3 discusses the design and fabrication process of Vivaldi, X-band horn, and double ridge horn antennas as well as their measurement results. Subsequently, Chapter 4 begins with waveguide measurements to investigate the electrical permittivity and the loss tangent of dielectrics that are used in the fabrication of the absorber. Furthermore, a free-space measurement setup that combines antennas and rotational stages is explained. Using this setup, performance metrics of the absorber under different oblique and polarization angles are measured and results are discussed. Last, optical measurements are presented to demonstrate the optical transmittance of the absorber in the visible range. As the last part of the thesis, Chapter 5 presents the conclusion and future outlook.

Chapter 2

Design, Simulation and Fabrication of Optically Transparent Metamaterial Absorbers

In this chapter, design, simulation, and fabrication of the proposed optically transparent metamaterial absorber are discussed. The transparent metamaterial absorber is desired to provide optical transparency together with a broadband microwave absorption. Furthermore, polarization insensitivity and robust performance under different oblique incidence angles are other important performance metrics. Our objective is to propose a thin and single-layer design that provides all the above-mentioned characteristics and outperforms similar designs available in the literature.

2.1 Design and Simulations of the Absorbers

We propose an optically transparent metamaterial absorber design that consists of top and bottom conductive layers and a substrate layer between them, as sketched in Figure 2.1. We used the same ITO film, which has 16 ohm/sq sheet resistance, for both the bottom and top layers. The bottom layer consists of a continuous ITO film that acts as a ground plane in the microwave regime. On the other hand, some parts of the ITO film for the top layer are etched to create desired patterns so that the impedance of the whole structure is matched with that of the free space, and the aforementioned performance metrics can be satisfied. Lastly, we choose PMMA, a transparent dielectric material, for the substrate layer. The electrical properties of PMMA are given as $\epsilon_r = 2.8$ and $tan\delta = 0.02$ for the 4-12 GHz.

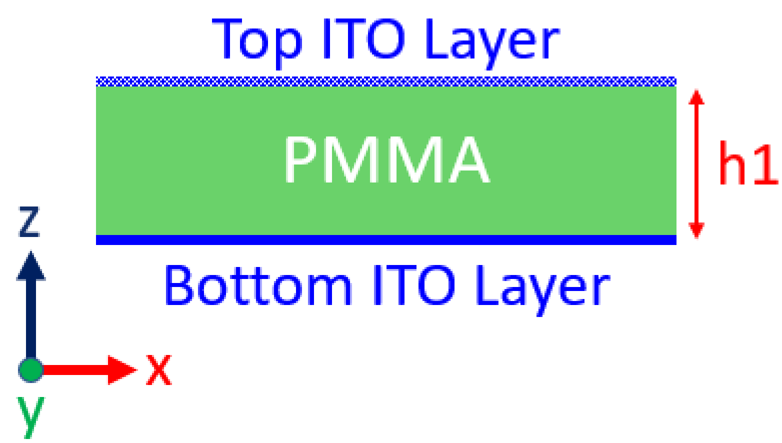

Figure 2.1: A side view of the generic architecture of our absorbers.

Regarding the design process for patterns of the top layer, a single square loop (SSL) unit cell was first considered as the initial design. We selected SSL unit cells due to their simplicity. However, these unit cells usually provide narrow-band absorption as presented in the literature [37], [38]. We show an SLL design in Figure 2.2, where $a = 8$ mm and $b = 1$ mm, and its absorption graph is given in Figure 2.3. The results show that the SSL has more than 90% narrow band absorption in two different frequency bands between 3.8-5.0 GHz and 10.0-12.4

GHz. Based on the result given in Figure 2.3, we decided to modify the SSL shape to obtain wide-band absorption (instead of working on multilayer designs, which increase the fabrication costs and yield accuracy problems).

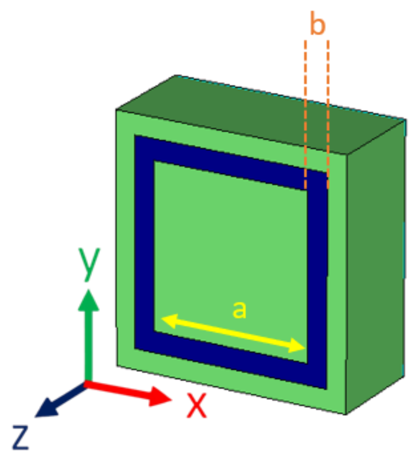

Figure 2.2: Our initial absorber design.

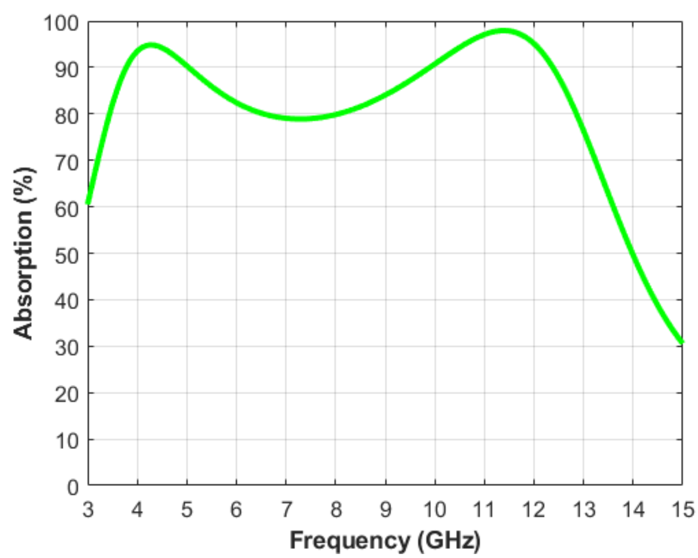

Figure 2.3: Absorption spectrum of our initial absorber design.

Therefore, 4 SSLs in a single unit cell design were considered as the starting modification as illustrated in Figure 2.4. Even if a single peak of absorption in the middle frequency band can be achieved, the goal of more than 90% absorption is not observed as shown in Figure 2.5. Next, 4 small SSLs, placed close to the corners and connected with a single and larger SSL in the middle, was introduced as shown in Figure 2.6. This modification results in more than 90% absorption in a broad band as displayed in Figure 2.7.

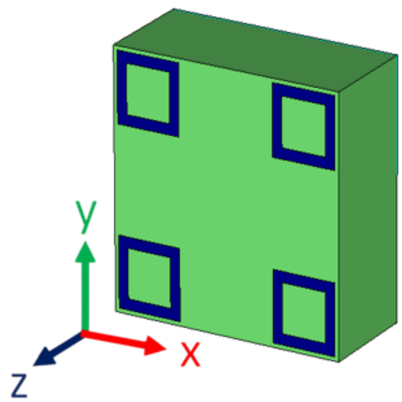

Figure 2.4: Four SLL design.

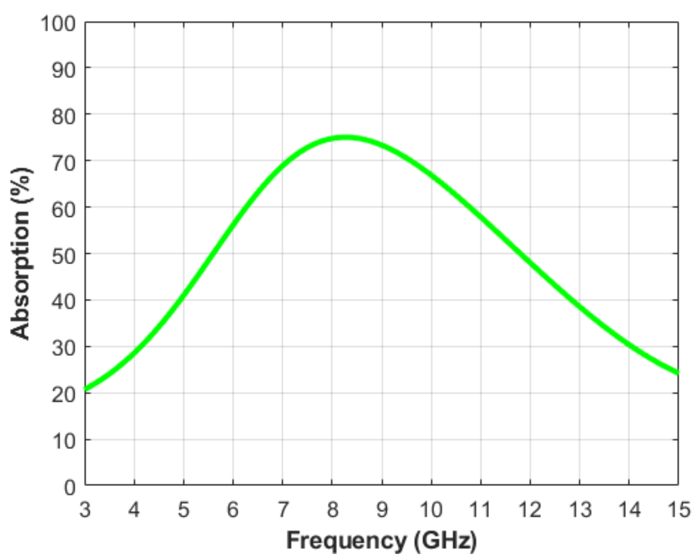

Figure 2.5: Absorption spectrum of four SLL design.

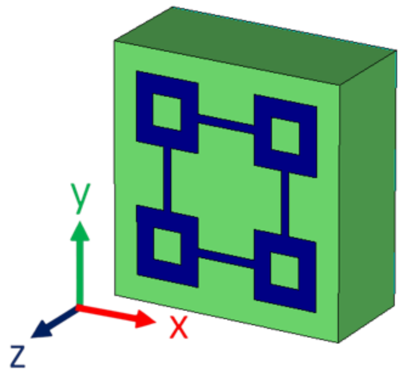

Figure 2.6: Initial modified SLL design.

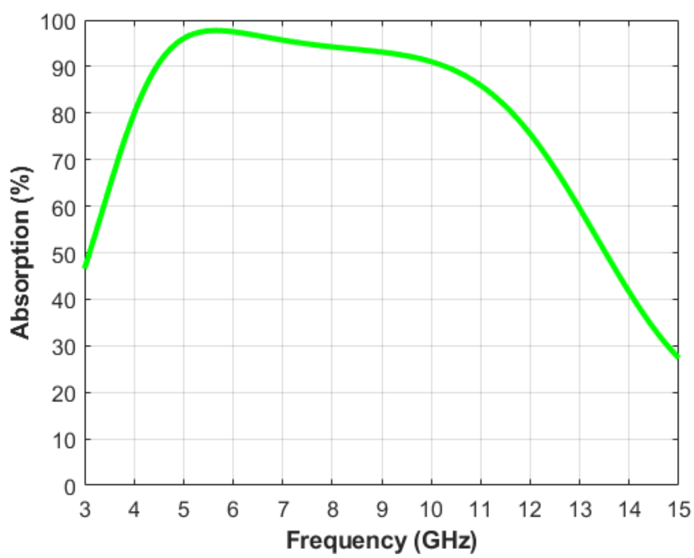

Figure 2.7: Absorption spectrum of the initially modified SLL design.

In order to obtain the optimized absorption response, several parameters of the design presented in Figure 2.6 are required to be optimized. Therefore, we created a MATLAB to CST interface for the optimization. This interface is based on a MATLAB plug-in consisting of visual basic (VBA) codes that allow to use all CST functions by writing MATLAB codes.

Initially, we fixed some of the design parameters due to the materials available at hand. These parameters are the size of one unit cell, the sheet resistance of the ITO films, and the permittivity and height of the dielectric PMMA layer. Thus, our algorithm solely focuses on the geometrical dimensions of the patterns shaped from the ITO film at the top layer of the design. First, we considered one eight (1/8) part of the top layer of one unit cell in the form of a 64×64 pixelated matrix that determines the presence/absence of ITO bricks. For instance, if a pixel has a value of 1, it means that the ITO brick is placed at that pixel location. We chose only the pixels in the first octant of the Cartesian plane (see Figure 2.8) in the algorithm. Pixels at other octants are determined based on the symmetry criterion. Thus, we took the first octant's vertical, horizontal, and diagonal symmetries to satisfy the polarization insensitiveness of the design.

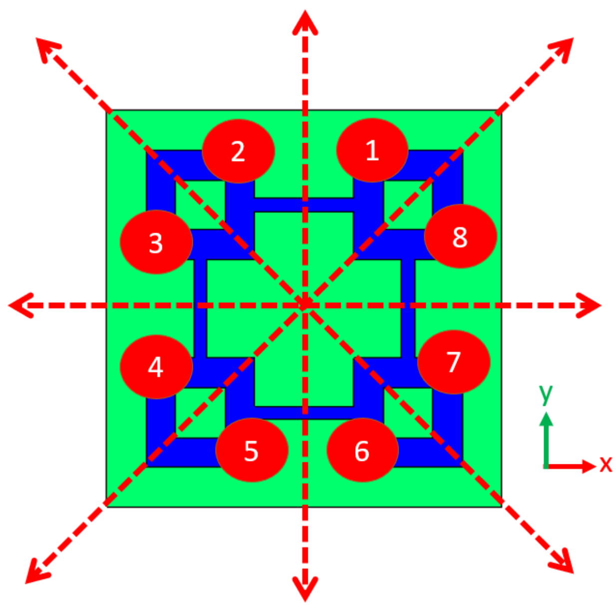

Figure 2.8: A unit cell separated into 8 octants.

We used particle swarm optimization (PSO) for the optimization of the first octant pixel values [40]. Parameter constraints were added to preserve the modified SLL shape. The simulations were continued until we reached the lowest thickness-to-bandwidth ratio across a wide absorption bandwidth. Based on the literature of a single-layer optically transparent absorbers, we targeted at achieving a thickness less than 0.08 λ_L (in terms of the longest operating wavelength), which we considered should be possible as this value is comparable to those of some available designs that provide more than 90% fractional bandwidth. After 500 simulations, the design that can satisfy both requirements was chosen as the best design (the first optimized design).

The simulations were conducted with the following CST Microwave Studio settings. We chose the frequency domain solver of the CST Microwave Studio because this solver supports unit cell simulations. Then, unit cell boundary conditions were used for lateral directions and open boundary conditions were selected for the vertical direction. When an open boundary condition is chosen, CST automatically assigns a Floquet port in the z-direction. We selected only propagating Floquet modes in the simulations. The frequency range was determined as the 4-12 GHz interval, which is the desired frequency band of the design and 1001 points were chosen for S-parameter data sampling. Afterwards, the structural design was modeled and materials were assigned. While modeling the structure, all the dimensions were parametrized to perform further optimizations.

The first optimized (PSO Structure I) design after PSO provided above 90% absorption in a fractional bandwidth of 91.1% for a thickness of 0.077 λ_L. However, this design has a level of absorption that stays barely above the 90% absorption threshold. Because of possible manufacturing imperfections, above 90% absorption might not be satisfied, and hence, another set of optimizations was conducted using PSO with a goal of increasing the absorption above 95% in the frequency 4-12 GHz band. As a result, the second optimized (PSO Structure II) design yielded more than 95% absorption in a fractional bandwidth of 69.4% with the same thickness. This result shows that the fractional bandwidth for more than 95% absorption in the case of PSO Structure II is improved compared to that of PSO Structure I, which has only 34.2% fractional bandwidth for absorption over 95%. On the other hand, PSO Structure II exhibits an absorption over 90% in a fractional bandwidth of 87.2%, which is slightly less than that of PSO Structure I, which provides 91.1% fractional bandwidth. In conclusion, above 95% absorption fractional bandwidth is significantly increased in PSO Structure II with a minor decrease in the above 90% absorption bandwidth. Table 2.1 provides the comparisons of the fractional bandwidths of these two designs. Furthermore, the 3D view of PSO Structures I and II are shown in Figure 2.9 and Figure 2.10, respectively. Lastly, CST simulation results of absorption for these two cases are provided in Figure 2.11. Final design parameters and dimensions are given in Figure 2.12, and Table 2.2, respectively.

Table 2.1: Fractional Bandwidth Comparison of PSO Structures I and II.

	Fractional Bandwidth (Above 90% Absorption) and Δf	Fractional Bandwidth (Above 95% Absorption) and Δf
PSO Structure I	91.1% (4.3-11.5 GHz)	34.2% (4.6-6.5 GHz)
PSO Structure II	87.2% (4.4-11.2 GHz)	69.4% (4.9-9.9 GHz)

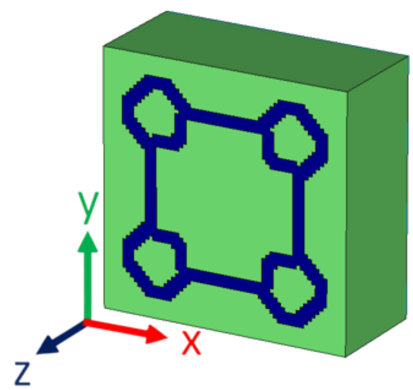

Figure 2.9: 3D view of PSO Structure I.

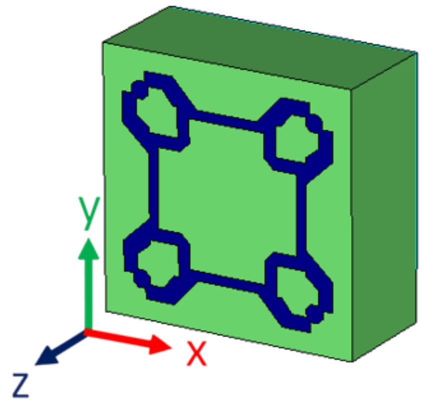

Figure 2.10: 3D view of PSO Structure II.

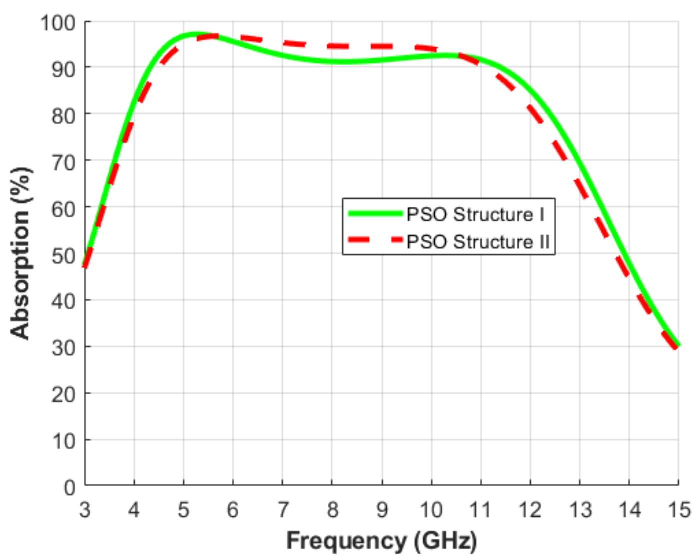

Figure 2.11: Absorption spectra of PSO Structures I and II.

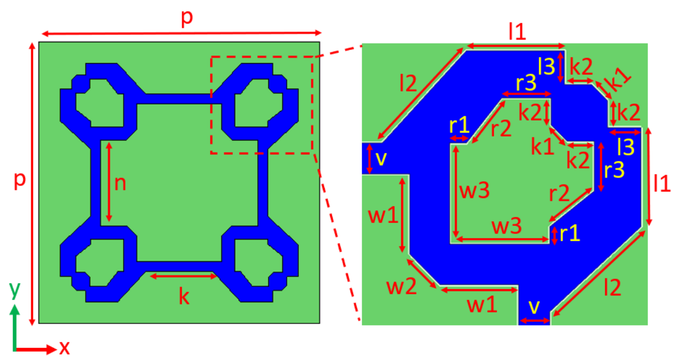

Figure 2.12: Geometrical parameters of the optically transparent absorber unit cell (PSO Structure II).

Table 2.2: Final dimensions of the optically transparent unit cell parameters (for PSO Structure II).

Parameter	Size (mm)
p	12.00
n	3.65
k	2.89
v	0.432
w1	1.11
w2	0.60
w3	1.40
r1	0.24
r2	0.77
r3	0.69
l1	1.375
l2	1.74
l3	0.47
k1	0.32
k2	0.375

Apart from the absorption results for normal incidence, the design was simulated for different polarizations and oblique incidence angles. Polarization-insensitiveness of the design is shown in Figure 2.13 for both TE and TM polarizations. On the other hand, the absorption response changes dramatically for different oblique incidence angles. For TE and TM polarizations, absorption spectra up to 60° oblique incidence angle are given in Figure 2.14 and Figure 2.15, respectively. For TE polarization, absorption remains more than 90% for angles up to 40°. On the other hand, even for a 60° oblique incidence angle, over

90% absorption was observed for TM polarization. Nonetheless, the absorption bandwidth decreases for higher oblique incidences.

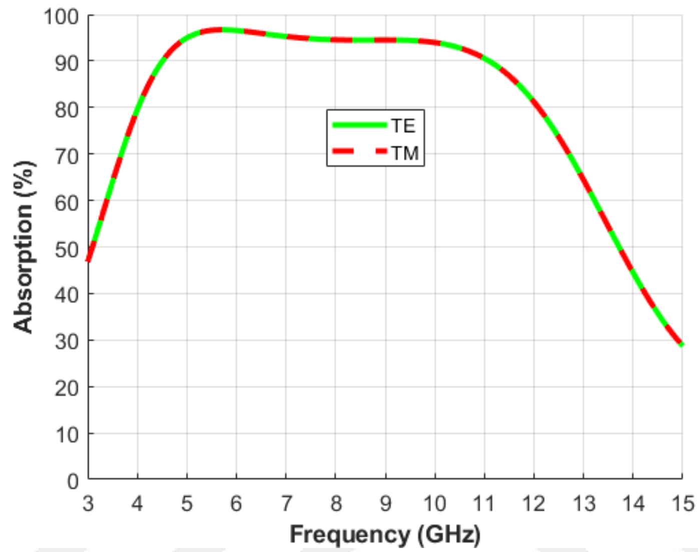

Figure 2.13: Absorption spectra of TE and TM polarizations under normal incidence.

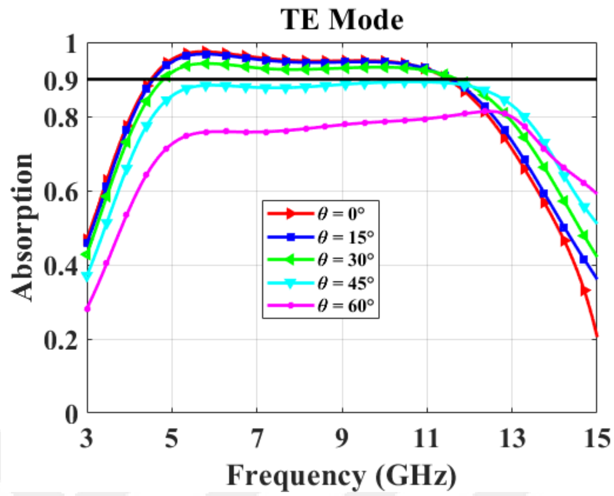

Figure 2.14: Oblique incidence simulation results for TE mode.

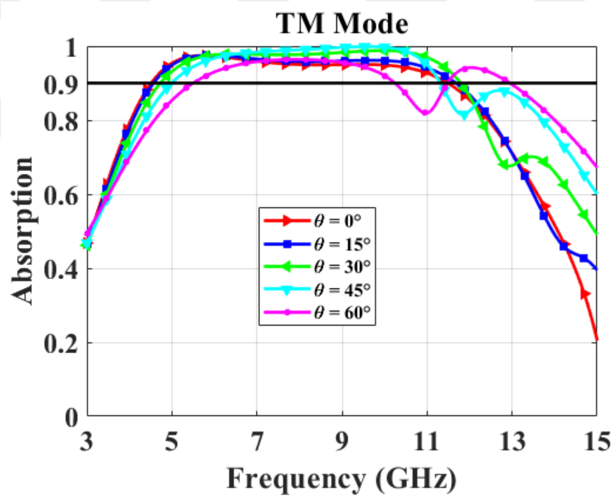

Figure 2.15: Oblique incidence simulation results for TM mode.

The equivalent circuit of the designed absorber may provide good understanding of the losses and the absorption mechanism and can lead to better future designs. In general, different unit cell types can be classified by their equivalent circuits based on the number of resonances. For instance, a double resonant unit cell structure was reported to be modeled as a parallel L-C circuit [41]. Furthermore, losses are represented by series resistors. As a result, resistors, inductors, and capacitors are used to make predictions for the top layer. Additionally, metamaterial absorbers have dielectrics integrated with a ground plane. The dielectric substrate is considered as a transmission line, and the ground plane stands as the short circuit.

To derive an equivalent circuit model of this absorber, surface currents of the top layer of the unit cell are illustrated in Figure 2.16. For TE polarization, the surface current is mainly distributed in the strips. Additionally, the current distribution is symmetric and in the same direction. This situation is similar to the single-layer square loop unit cell designs in [42].

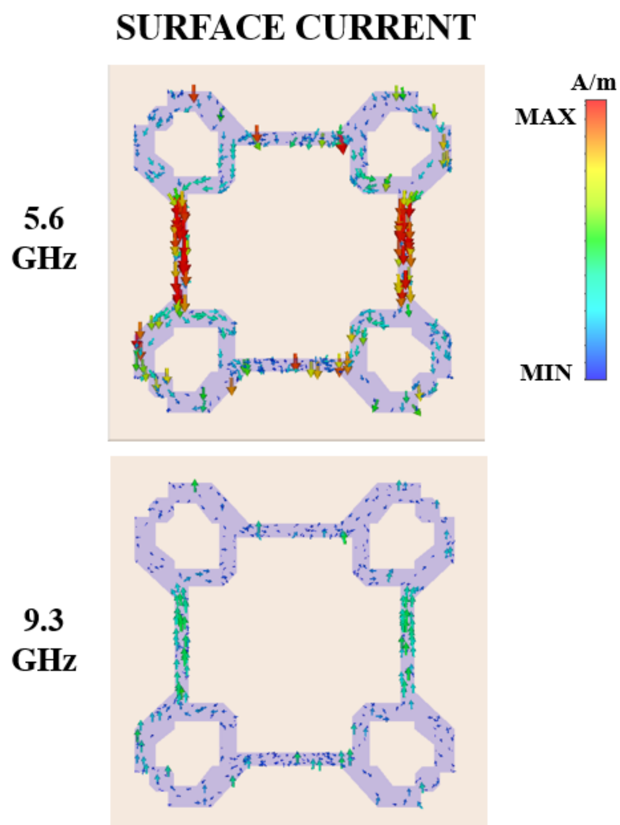

Figure 2.16: Surface current of top layer for 5.6 and 9.3 GHz.

Due to our design's single-loop nature, a single R-L-C circuit can be considered as the equivalent circuit of our unit cell's top layer. Furthermore, a transmission line representing the dielectric layer and a ground plane acting as a short circuit are considered as depicted in Figure 2.17. To determine the values of the equivalent circuit model, advanced design system (ADS) was used. The initial values of R, L, and C were calculated from sheet resistance, frequency, and geometrical parameters [42]. Then, we determined the latest values using a curve-fitting technique. It is found that $R_1 = 357\ \Omega$, $C_1 = 73.1$ pF, $L_1 = 7.8$ nH and $h_1 = 5.4$ mm. We compared the equivalent circuit model results with those obtained from the CST simulations in Figure 2.18.

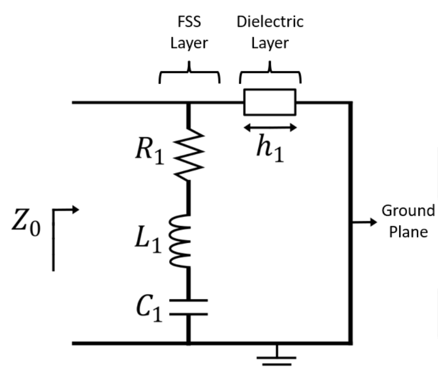

Figure 2.17: Equivalent circuit model of the optically transparent absorber.

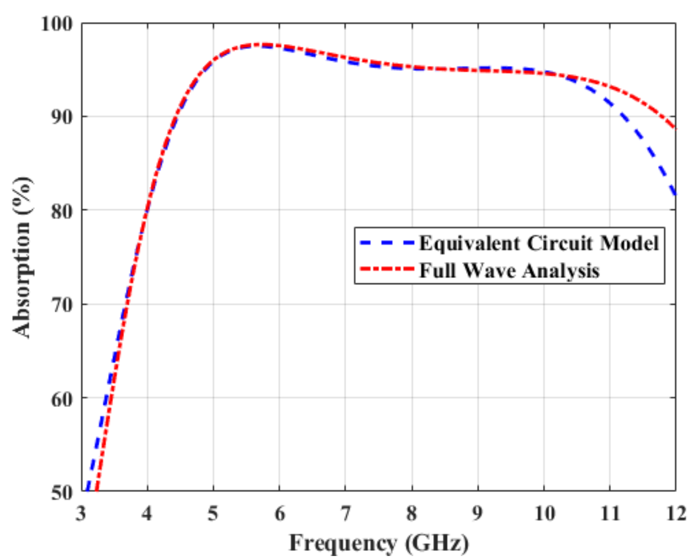

Figure 2.18: Comparison of absorption results obtained from the equivalent circuit analysis and the full wave analysis.

2.2 Fabrication of the Absorber

As described previously, the proposed absorber consists of top and bottom ITO-coated PET films along with a dielectric layer as PMMA between them. The ITO film has 16 ohm/sq sheet resistance. As the initial fabrication step, bonding an ITO-coated PET film to the PMMA using several glues and tapes such as double-sided transparent tape, UV-curable glue, washable glue, and epoxy glue were tried. The UV-curable and washable glues were unsuccessful in bonding PMMA to PET film, and double-sided tape had worse optical transparency than the epoxy glue. As a result, the epoxy glue was decided to be the best option due to its high transparency, strong bonding, and quick drying time.

After the bonding stage, PET-attached PMMA was placed under the CNC-controlled 355 nm laser source. This laser source can send extremely short pulsed beam for processing on micro-machining, marking, and other applications [43]. Here, the laser source was used to etch the ITO in order to make the desired pattern for the top layer by shining short pulses on the desired locations. However, during the etching process, PMMA and PET layers under ITO must not be damaged. At 355 nm wavelength, according to [44], the absorption rate of PET is around 1/1000 of the ITO absorption rate. Thus, the laser light absorbed in the PET film does not damage or change the properties of the PET [44]. In the literature, laser energy and speed are reported to be the most critical parameters in the ITO etching using a nanosecond laser [45]. Increasing the laser energy can damage ITO and no removal of ITO can be observed for lower energy levels. Furthermore, when the laser scans at lower speeds, overlapping areas are found and complete removal of ITO is achieved. We optimized these parameters in the fabrication process and measured the resistance of the etched places using a digital multimeter. We observed more than 1 Mohm resistance, which shows that the laser light can successfully remove conductive ITO from PET film since non-etched parts have less than 100 Ohm resistance. During the etching process, due to the limits of the CNC-controlled laser source setup, only an 8 cm by 8 cm area was processed at each time. After the etching process was finished for this area, the sample was moved using the CNC setup software. In the end, a total area of 20 cm by 20 cm was processed. As the last fabrication step, we attached another PET film to the PMMA as a ground layer. The fabricated prototype can be seen in Figure 2.19. One unit cell under the optical microscope is shown in Figure 2.20.

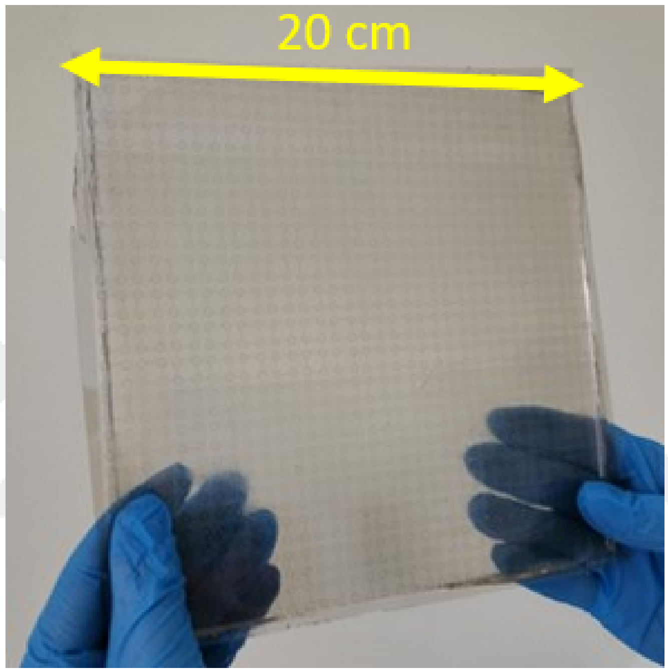

Figure 2.19: Fabricated optically transparent absorber.

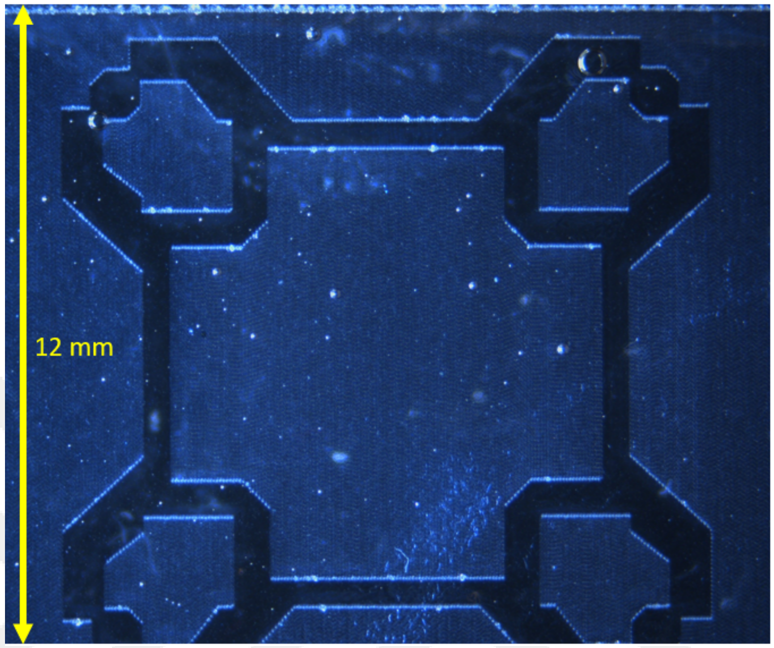

Figure 2.20: One unit cell view of the optically transparent absorber under optical microscope.

Chapter 3

Design, Fabrication, Simulation and Measurement of Antennas

In this chapter, design, simulation, fabrication, and experimental results for three different antenna types are investigated. We have chosen a Vivaldi, a standard pyramidal horn, and a double ridge horn antenna due to their extensive use in EMI/EMC, radar, wireless, and, most importantly, absorber measurements since they exhibit a high operation bandwidth, low side lobe levels, and a relatively highly directive radiation pattern [46]. The wide operation bandwidth nature of these antennas allows us to use a single antenna in the absorption measurements instead of several antennas, each of which works across a different frequency band. Additionally, the directive pattern of these antennas is important in terms of reducing the interference of the environmental effects during the measurements. Furthermore, these antennas are cost-effective.

3.1 Vivaldi Antennas

Vivaldi antennas are commonly referred to as tapered slot antennas, which exhibit perfect radiation characteristics with high gain, broadband performance, constant beamwidth, and low cross-polarization [47]. Furthermore, these antennas can be fabricated with a planar circuit board technology (PCB), which allows for simple and fast fabrication. Thus, we initially considered Vivaldi antennas as one of the suitable choices for our absorber measurements.

3.1.1 Vivaldi Antenna Design

Vivaldi antenna types can be classified as coplanar, antipodal, and balanced antipodal Vivaldi antennas. In a coplanar Vivaldi antenna, two radiator planes are on the same side of the substrate, and it is fed via aperture coupling. On the other hand, antipodal Vivaldi antennas are printed on both top and bottom layers of the substrate and are tapered in opposite directions which allows to solder standard SMA connectors [48]. The antipodal Vivaldi antennas offer a much wider frequency band than the coplanar Vivaldi antennas do [49]. In the case of the balanced Vivaldi antennas, it is possible to reduce the level of cross polarization in comparison to other Vivaldi antenna types. However, these require multiple copper layers and dielectric substrates [50]. Due to the complex fabrication processes of the balanced antipodal Vivaldi antennas and lower operating bandwidth of the coplanar Vivaldi antennas, the best option for our measurements was to use an antipodal Vivaldi antenna (AVA).

AVA operates as a resonant antenna at lower frequencies and a traveling wave antenna at higher frequencies (current wave travels on each arm) [51]. These traveling current waves across each arm have a phase difference of 180°, which creates radiation in the end fire direction in a wide bandwidth and these arms are created in the form of exponential tapers with the following relation:

$$y(x) = \pm A e^{(px)} \tag{3.1}$$

where y is half of the separation of the arms, x is the location in the length of the antenna, A is half of W, which is the width of the microstrip part, and p is the taper rate [47]. The arms are shown in Figure 3.1 with the curve a and curve b. Apart from the arm parts, a feeding section that consists of double-sided parallel strip lines with a width of Wf must be designed. Furthermore, the strip lines must have a particular ground plane. To design the ground plane, a transition section is required. For instance, an elliptical transition can be added to one layer to obtain the desired ground plane [52]. This transition converts double-sided parallel strips into microstrip lines to which a standard SMA connector can be soldered. In Figure 3.1, the elliptical transition in the ground plane as the curve d is illustrated.

We employed the AVA design given in [53], which works in the frequency range of 4-12 GHz. This frequency band covers the entire operating frequency band of the fabricated absorber. We used FR-4 with a thickness of 1.6 mm as the dielectric substrate because it is available and cheap.

Note that AVAs can be bulky when an ultrawideband performance is required. Some modifications such as etching symmetrical slots between the arms to miniaturize the antenna were previously reported [54]. In our AVA design, these slots helped us to achieve an ultrawideband operating frequency range even for a small-sized antenna. These slots namely S1, S2, and S3 are also depicted in Figure 3.1.

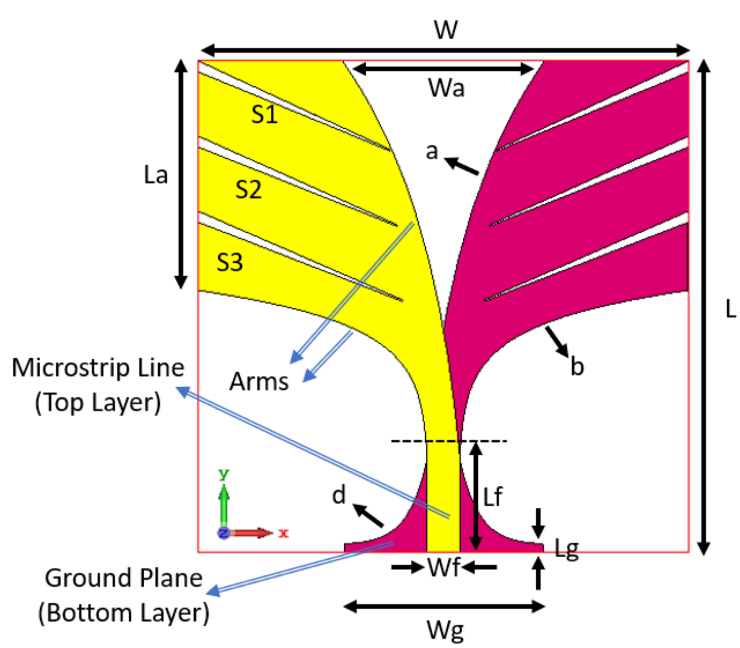

Figure 3.1: AVA design.

Next, we used CST Microwave Studio for the analysis of the antenna where

Table 3.1: Dimensions of the AVA.

L	W	Wa	Wg	Wf	La	Lg	Lf
36 mm	36 mm	14.8 mm	14.6 mm	2.4 mm	16.8 mm	0.6 mm	7 mm

dimensions are provided in Table 2.1. We used the time domain solver option of the CST Microwave Studio with a discrete port. The discrete port was placed between the top and bottom copper layers and normalized to 50 Ohm. -60 dB accuracy was required to complete the simulations. Furthermore, we set the open boundary conditions in all directions. The frequency range was 3-12 GHz and a broadband far-field monitor was set. This monitor is usually used to calculate the directivity and realized gain. Figure 3.2 illustrates that realized gain results from [53] and the CST simulation results agree fairly well with each other. However, there is a significant discrepancy when the $|S_{11}|$ results are compared as shown in Figure 3.3. Fortunately, both of them are less than -10 dB throughout the entire 4-12 GHz frequency band. Different simulation settings, using a discrete port instead of feeding with SMA connector via a waveguide port (may be used in [53]), and probably unreported details in [53] can be very important and may cause such a discrepancy.

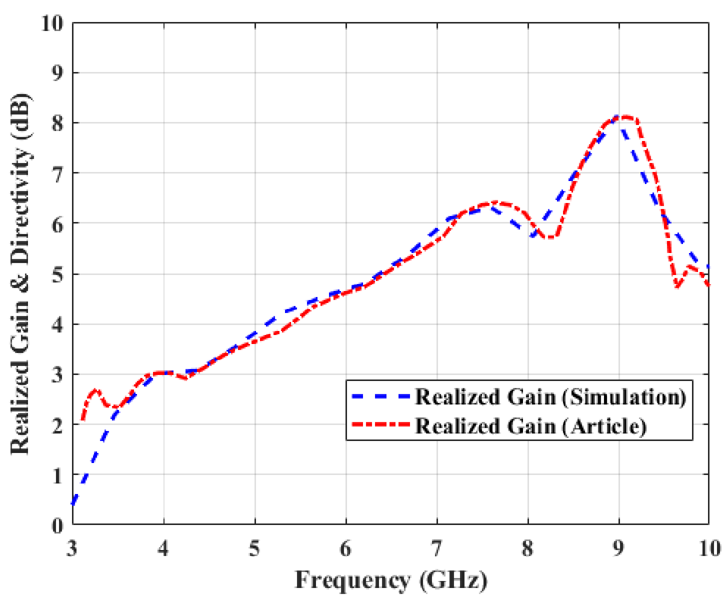

Figure 3.2: Simulation results of the realized gain reported in [53] and obtained from our CST Microwave Studio simulations.

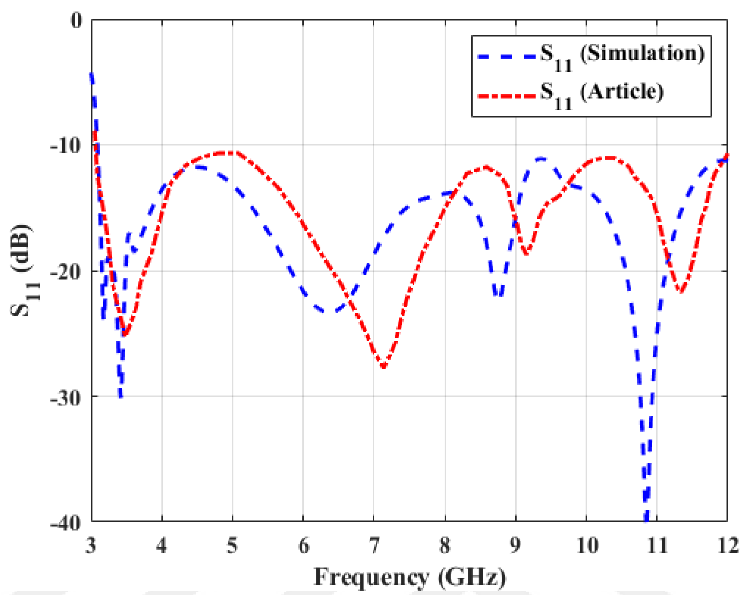

Figure 3.3: Simulation results of S_{11} reported in [53] and obtained from our CST Microwave Studio simulations.

3.1.2 Vivaldi Antenna Fabrication and Measurement

As discussed in the design part of AVA, we used 1.6 mm thick FR-4 plates covered with 0.35 mm thick copper on both top and bottom sides. We used LPKF Protomat PCB Milling Machine for copper etching based on the Gerber files that provide the necessary information for the desired geometrical shapes on both layers. Afterward, we soldered a standard SMA connector. The fabricated AVA is shown in Figure 3.4, and finally Figure 3.5 presents the measured $|S_{11}|$ results of the fabricated AVA. It can be seen that $|S_{11}|$ < -10 dB throughout 3-12 GHz band.

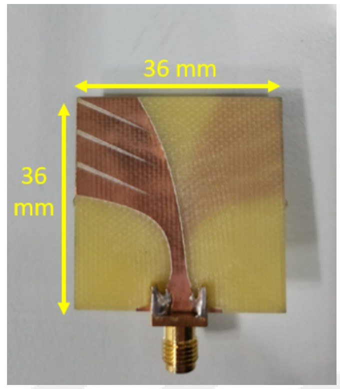

Figure 3.4: Fabricated AVA.

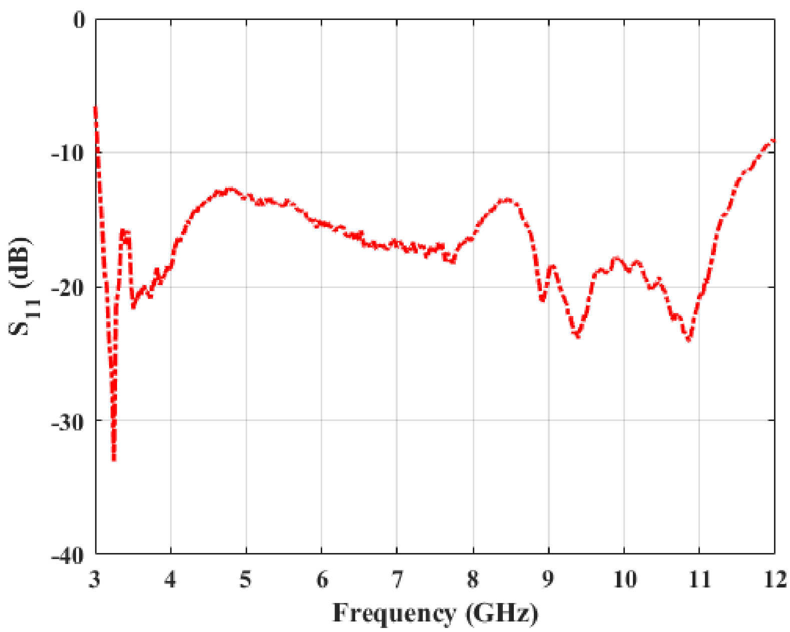

Figure 3.5: Measured S_{11} spectrum of the fabricated AVA.

3.2 Horn and Double Ridge Horn Antennas

Even if the fabricated AVA provides ultrawide bandwidth with a small size, the integration of this antenna to our measurement setup turned out to be problematic. Especially aligning it while changing the antenna position was very challenging. Thus, we decided to design and fabricate a standard horn and a double ridge horn antennas due to their mechanical stability and extended sections that allow us to fix them on our optical table on which our measurement setup is prepared.

Standard horn antennas are widely used in many measurements for antennas or absorbers under test and available designs including their modified versions such as corrugated horn and double ridge horns are available. Particularly, the double ridge horn antennas are extensively used owing to their extensive bandwidth, higher gain, and relatively narrow beam [55]. Unfortunately, the double ridge horn antennas require a significantly complex fabrication procedure. Thus, we first built a standard pyramidal horn antenna which has small dimensions and less complex design as the starting point to optimize the fabrication procedure. Then, using the experience we gained, we constructed a double ridge horn antenna, which has a much higher bandwidth compared to that of the standard pyramidal horn antenna.

3.2.1 Standard Pyramidal Horn Antenna Design

Standard pyramidal horn antennas are designed based on the idea that a rectangular waveguide is gradually transitioned into a horn and the transition section provides an impedance matching from the waveguide to the free space [56]. Our aim was to design a pyramidal horn antenna that works in the X-band (8.2-12.4 GHz frequency range). X-band coincides with a portion of our designed absorber's operating frequency range. We used Matlab antenna toolbox to calculate the dimensions of the X-band horn antenna and performed the full wave simulations using the CST Microwave Studio. The position and length of the inner conductor of the SMA connector that is needed for feeding the antenna, were optimized. In CST, we fed the SMA connector with a waveguide port. We used the same simulation settings that we used for the AVA in the 8-12 GHz frequency range. The overall and the 2-D half views of the designed standard pyramidal horn antenna are depicted in Figure 3.6 and Figure 3.7, respectively. Table 3.2 provides the final dimensions of the designed antenna.

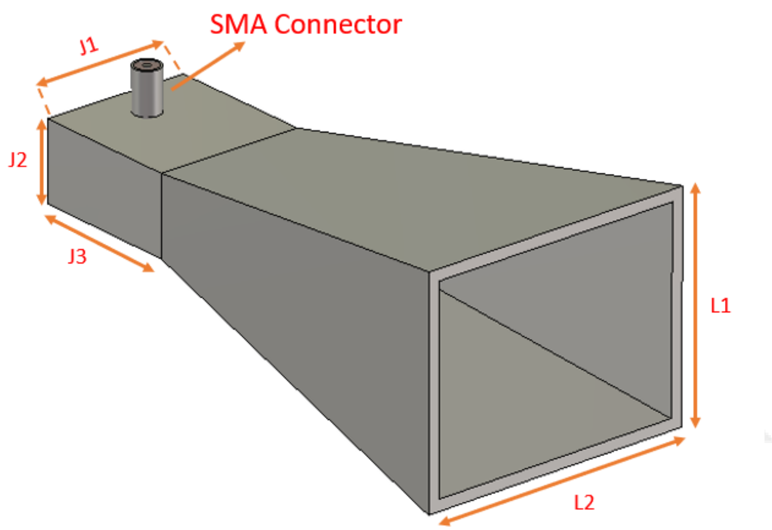

Figure 3.6: X-band standard pyramidal horn antenna design.

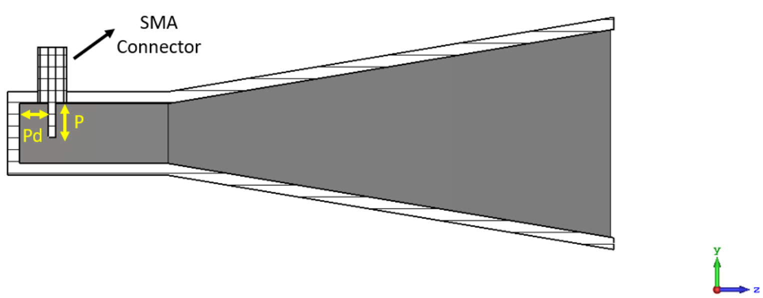

Figure 3.7: X-band standard pyramidal horn antenna half view for showing SMA connector position.

Table 3.2: Final dimensions of the standard pyramidal horn antenna.

J1	J2	J3	L1	L2	Pd	P
14.2 mm	14.2 mm	27.2 mm	39.6 mm	49.7 mm	4.9 mm	5.7 mm

3.2.2 Standard Pyramidal Horn Antenna Fabrication and Measurement

Many different fabrication processes and detailed fabrication steps for horn antennas are available in the literature. Recently, adopting fused deposition modeling (FDM) 3D printing technology into antenna fabrication especially for horn antenna that uses plastic filaments and post-metallization processes has become popular [57], [58]. Therefore, we decided to employ this 3D printing technology to fabricate our horn antenna as it is a simple, cost-efficient and rapid process. Briefly in this technology 3D printers use thermoplastic filaments heated to the melting temperature and extruded layer by layer to fabricate the 3-dimensional features [59]. Yet, several parameters are needed to be determined to optimize the fabrication process. These parameters can be categorized as slicing parameters, building orientation, and temperature conditions of the bed and the filament. Slicing parameters can be further detailed as deposition speed, infill, layer thickness, and nozzle diameter [60]. Once we finished our optimization on the aforementioned parameters, we applied post-processing, which consists of removing support layers and increasing the smoothness and adhesion of the surfaces. Finally, in the last step, we applied coatings to make the printed prototype conductive. We fabricated several X-band pyramidal horn antennas to optimize the printing parameters and the post-processing and coating stages.

To begin with, horn antennas that we simulated using the CST Microwave Studio were redrawn in Solidworks 2019. This allowed several features to be added to the antenna drawing. Initial drawing of the horn antenna was the same as that of the simulated one, as shown in Figure 3.8. However, fabricating this antenna would create difficulties in the post-processing and coating stages of inner surfaces. Hence, we separated the antenna into two halves to increase the ease of coating, as half of it is depicted in Figure 3.9. Yet, perfectly bonding these half-pieces emerged as another problem. To overcome this problem, we considered using screws and nuts as a solution. Then, we added pieces with screw holes to the near edges of the design, as shown in Figure 3.10.

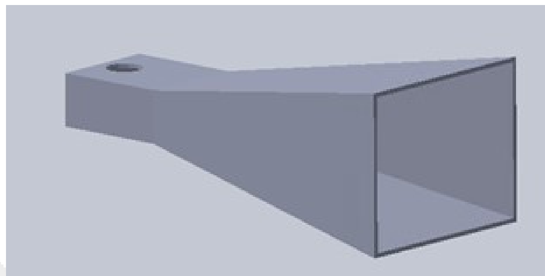

Figure 3.8: Initial drawing of the X-band standard pyramidal horn antenna.

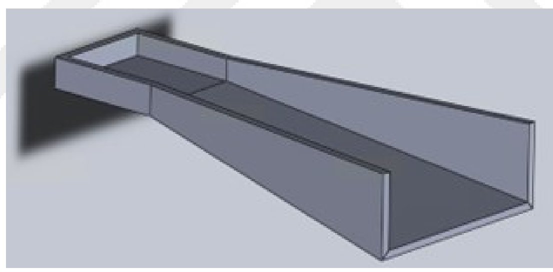

Figure 3.9: Semi-part drawing of the X-band standard pyramidal horn antenna.

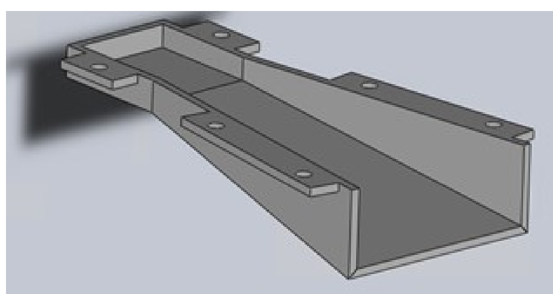

Figure 3.10: Semi-part of the X-band standard pyramidal horn antenna with screw mountable pieces.

Lastly, because this antenna was to be fixed on the optical table, we added pieces with screw holes that are compatible with optical table components. In addition, we aligned these holes horizontally on the same line and arranged the distance between the holes as the multiples of 2.5 cm, which is the center-to-center pitch between two adjacent holes on an optical table. A complete design including the distances between the holes is provided in Figure 3.11, in which yellow boxes illustrate the screw holes that can be used with optical table stages. Figure 3.12 shows the fabricated antenna fixed on the optical table with optical table stages and screws.

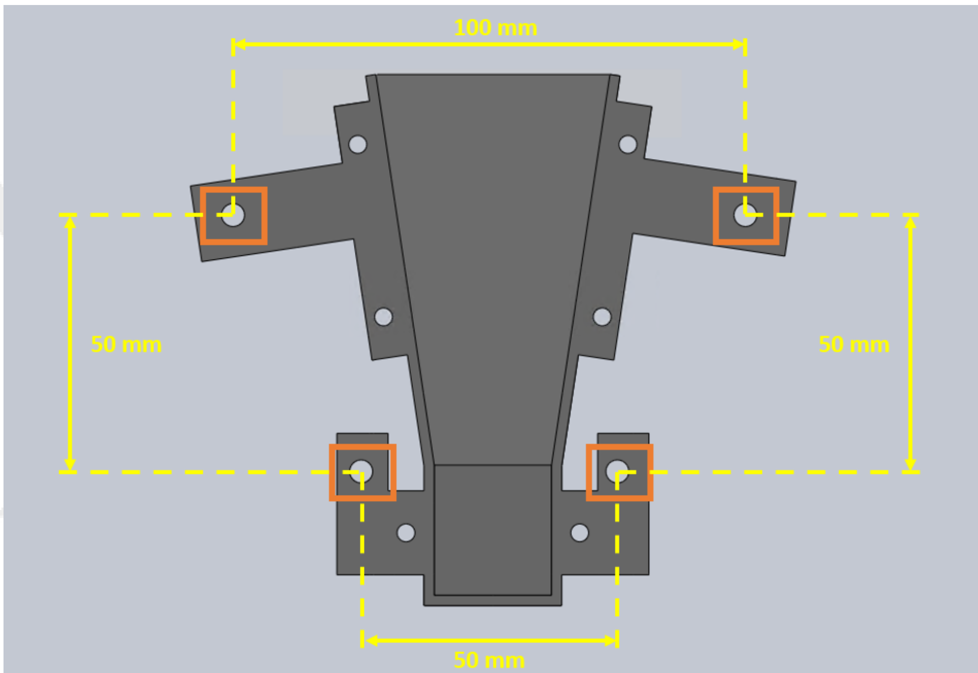

Figure 3.11: Final antenna drawing to be fixed on the optical table with optical stages and screws.

After the drawing process with Solidworks was finished, we determined 3D fabrication parameters. First, slicing parameters were taken into consideration. Since only a 0.4 mm nozzle is available at our lab at UNAM, we could not change the nozzle. We used default deposition speed and wall thickness as 50 mm/s and 0.8 mm, respectively. To increase the mechanical strength, we set the thickness of each antenna layer as 3 mm. The infill ratio was optimized as 20% to reduce printing time. We concluded that increasing this value did not change the mechanical strength significantly but increased the printing time tremendously. We used 1.75 mm PLA filament for all fabrications. Based on the numbers provided by the filament manufacturer, 210 °C was chosen for filament temperature. Since we used PLA filament, there is no need to provide bed temperature. However, the bed temperature has a direct influence on the adhesion between the first layer

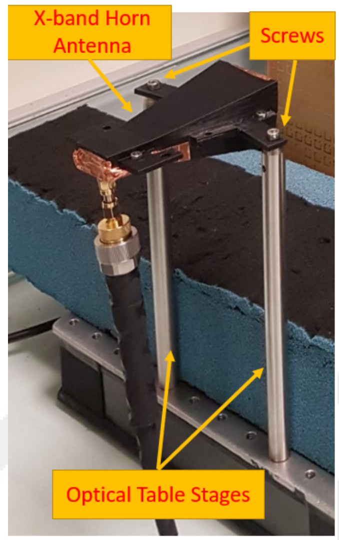

Figure 3.12: Fabricated X-band standard pyramidal horn antenna fixed on the optical table.

and the printing bed and setting a bed temperature allowed for better sticking of filaments to the bed [61]. Thus, after trial and error, we set the bed temperature to 60 °C. Furthermore, we optimized the orientation of the designs during the fabrication. First, we considered the horizontal placement of the designs. By doing so, printing stayed close to the bed and achieved better sticking. Yet, the surfaces of the fabricated pieces were worse than expected. To solve this problem, we used vertical placement. Even if sticking was worse, surfaces became significantly smoother. To further increase the sticking, we cleaned the bed surface each time before printing. Horizontal and vertical alignment comparison of printed examples can be seen in Figure 3.13.

The last stages of the fabrication process include post-processing and coating. Post-processing can be conducted by wet and dry sanding together with primer spraying. First, we rubbed each surface with sandpapers of 100 and 200-grit sizes. This procedure removed possible surface errors and resulted in a better smoothness for the surfaces. Then, we sprayed a primer everywhere to fill the small gaps and created surfaces that are easier to coat. However, spraying was not balanced on each face and created small cracks in some locations. We applied wet sanding with 500 and 1200-grit sandpapers to overcome these problems. The

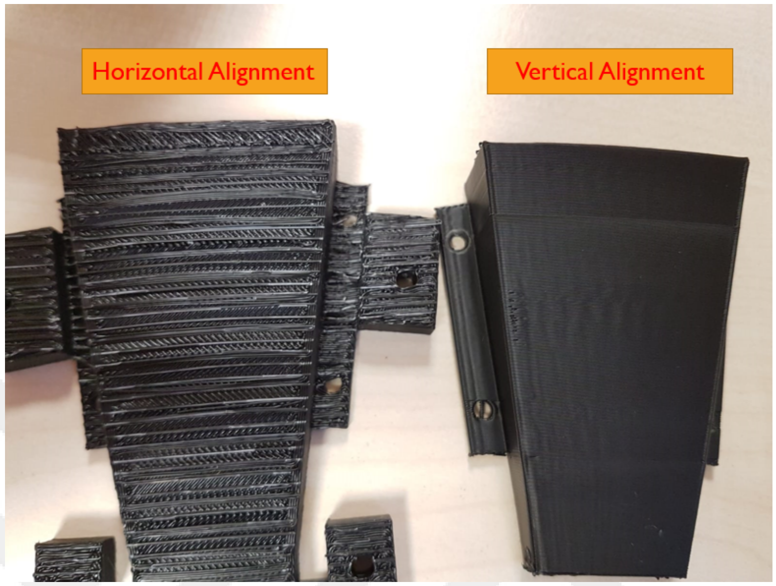

Figure 3.13: Comparison of alignments in the fabricated antenna samples.

result of each process is illustrated in Figure 3.14. After this post-processing, copper spraying was applied on the printed pieces to make conductive faces. The picture of a copper spray-coated X-band horn antenna is displayed in Figure 3.15.

Figure 3.14: Post-Processing of 3D printed pieces.

The measured $|S_{11}|$ of the fabricated antenna is presented in Figure 3.16. Unfortunately, the experimental results are worse than those of the simulated ones. $|S_{11}| > -10$ dB at certain frequencies in the desired frequency range. Problems during the fabrication process such as possible differences between the simulated and fabricated dimensions, the position of the SMA connector and unsmooth antenna surfaces can be the reasons for worse measured $|S_{11}|$ results.

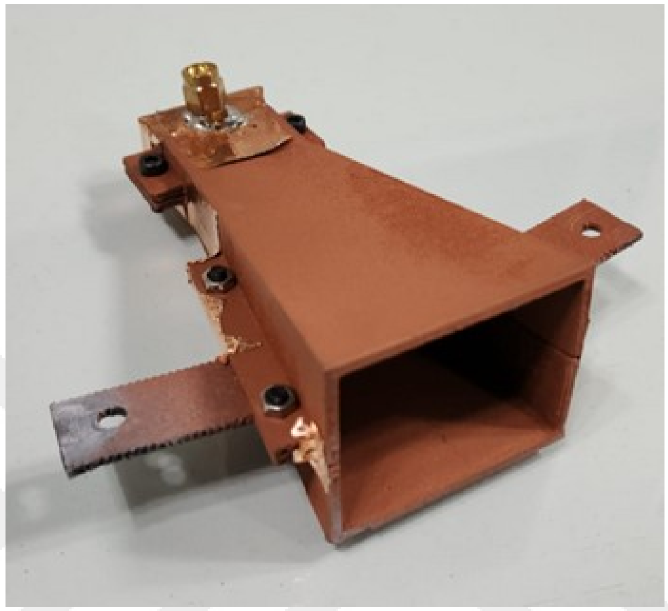

Figure 3.15: Fabricated X-band standard pyramidal horn antenna.

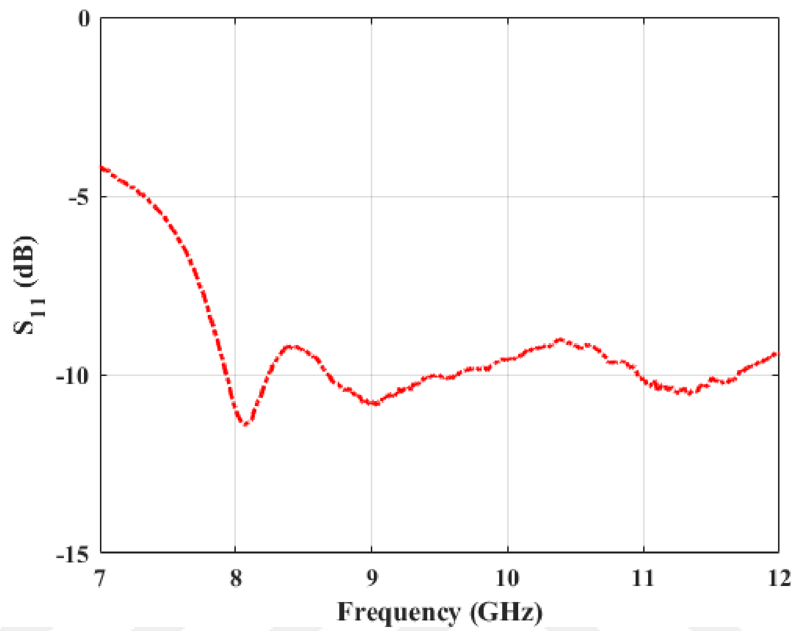

Figure 3.16: Measured S_{11} results of the X-band standard pyramidal horn antenna.

3.2.3 Double Ridge Horn Antenna Design

The double ridge pyramidal horn antenna is a type of pyramidal horn antenna that has internal ridges [56]. This antenna provides a higher bandwidth because the ridges in the waveguide section produce capacitive effects, and hence, the cut-off frequency of the waveguide is reduced [62]. Thus, the ridge waveguide eliminates higher-order mode propagation and increases single-mode bandwidth [63]. Consequently, we designed a double ridge horn antenna that can cover 4-12 GHz frequency range to be used for our absorption measurements.

The double ridge horn antennas can have different ridge profiles, such as linear, quadratic, exponential, and Gaussian ones for the impedance matching between the waveguide feeding section and the free space [64]. For the feeding section, coaxial to the double ridge waveguide feed must be designed. An SMA connector can be connected to the waveguide section and lower return loss can be obtained with the optimum back cavity dimensions and SMA connector spacing [63].

The double ridge horn antennas have a transition or a flare section for impedance matching between the waveguide and the free space. We used HFSS antenna toolkit to find the flare section dimensions, which are based on the radiation frequency provided by the user. In the designed antenna, 2 GHz was chosen as the minimum frequency of radiation. As shown in Figure 3.17, the toolkit calculates the aperture and ridge profile dimensions based on this minimum frequency value. Then, an antenna is automatically drawn in HFSS, as depicted in Figure 3.18.

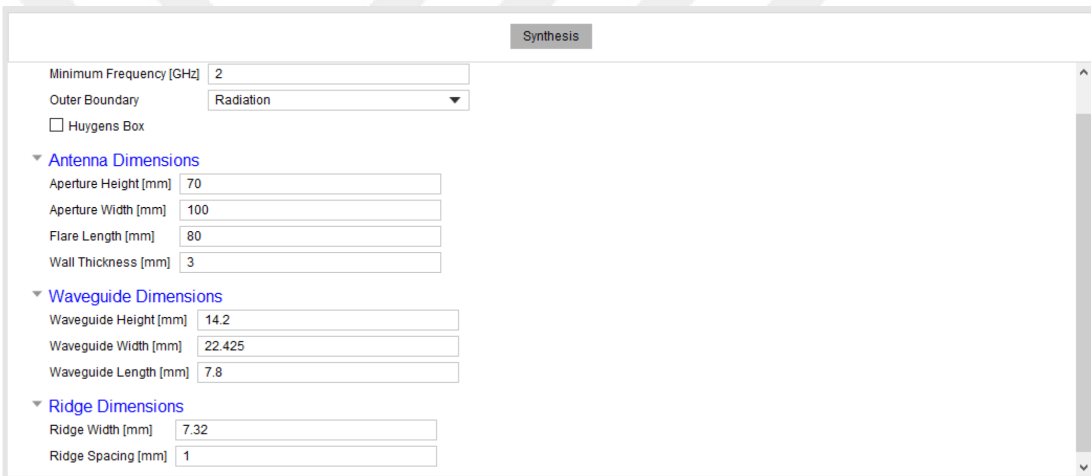

Figure 3.17: Double ridge horn antenna parameter synthesis.

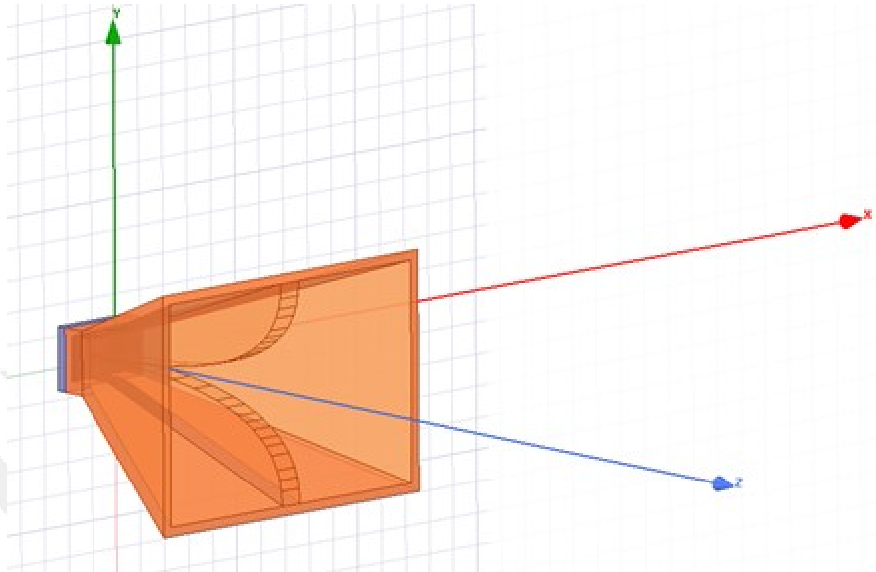

Figure 3.18: Double ridge horn antenna drawn in HFSS.

However, the HFSS antenna toolkit does not provide the dimensions of the feeding section of the antenna. Thus, a feeding section, which consists of an SMA connector and a double ridge waveguide, must be separately designed and attached to the rest of the antenna. The outer conducting part of the SMA connector is connected to the outer part of the antenna. With the help of the dielectric part between the inner and outer conducting parts of the SMA connector, we connected the inner conductor to the lower ridge of the antenna. The side view that shows the SMA connector connection is provided in Figure 3.19.

We used the same simulation settings that we previously used for the pyramidal horn antenna part and performed simulations to optimize the length of the waveguide, the position of the SMA connector, and the length of the cavity after the waveguide. We noticed that firstly without changing the distance between the end of the waveguide and the backside of the antenna (shown as P in Figure 3.19), if we increase the waveguide section length (shown as W3 in Figure 3.20), the bandwidth of the antenna decreases. However, special care is required because if W3 is decreased too much, the inner conductor of the SMA connector would be disconnected from the lower ridge of the antenna. Secondly, reducing the length of the cavity backside part (reducing distance P in Figure 3.19) without changing the waveguide dimensions (W3 in Figure 3.20) causes the antenna to radiate at lower frequencies. Lastly, the effects of the position of the SMA connector must be investigated. We found that bandwidth and return loss values change tremendously for different positions of the SMA connector. Thus, we chose the SMA position such that it provides the highest bandwidth and the lowest return loss. The final antenna design and its dimensions are presented in Figure 3.20 and Table 3.3, respectively.

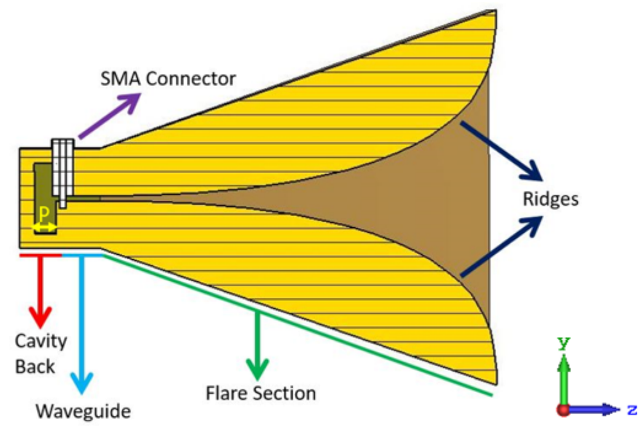

Figure 3.19: Side view of the double ridge horn antenna along with the SMA connector connection.

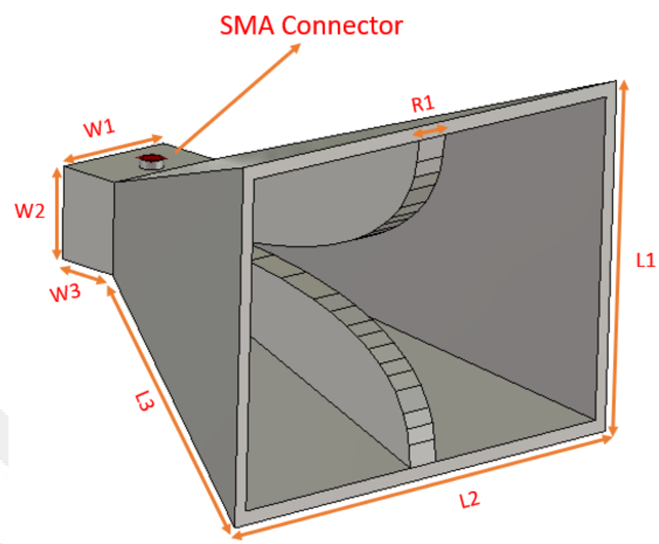

Figure 3.20: Finalized double ridge horn antenna design (with the parameters tabulated in Table 3.3).

Table 3.3: Final dimensions of the double ridge horn antenna.

P	W1	W2	W3	L1	L2	L3	R1
4.2 mm	28.4 mm	20.2 mm	15.7 mm	76 mm	106 mm	93.2 mm	7.3 mm

3.2.4 Double Ridge Horn Antenna Fabrication and Measurement

After completing the simulations, we drew the designed antenna with Solidworks as depicted in Figure 3.21 and used the optimized 3D fabrication parameters that were previously determined in the standard pyramidal horn antenna fabrication process. Then, we applied copper spray to the pieces and soldered an SMA connector. The fabricated antenna is shown in Figure 3.22.

Due to the more complicated design of the double ridge horn antenna compared to the standard pyramidal horn antenna, several problems were encountered in the fabrication stage. First, the ridge profile part had an unsmooth surface and required a careful sanding process. Second, spray coating of the waveguide section needed a careful treatment since the dimensions were very small. Last, spray

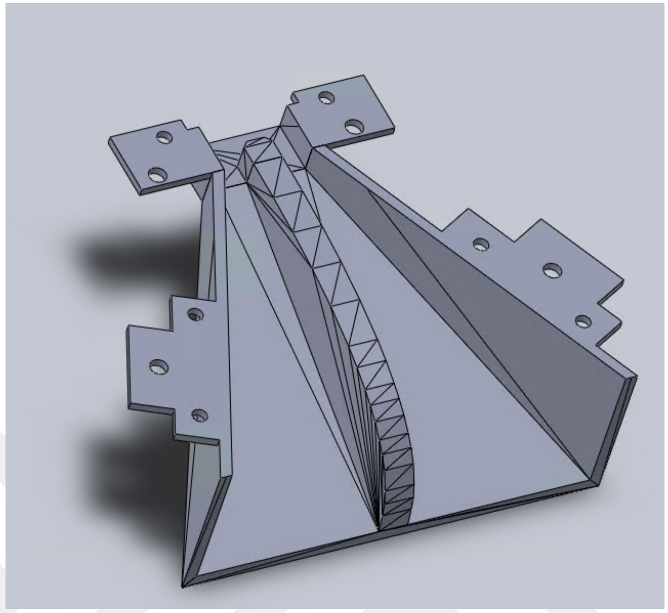

Figure 3.21: A complete design of semi-part of the double ridge horn antenna.

coating for the antenna was conducted three times to increase the conductivity of the surfaces. After the coating process, the edges had some cracks. Thus, copper tapes were used in these places as can be seen in Figure 3.22.

The measured $|S_{11}|$ spectrum is presented in Figure 3.23. It can be seen that, although we desire $|S_{11}| < -10$ dB in the 3-12 GHz range, imperfections in the fabrication process resulted in $|S_{11}| < -10$ dB (slightly over -10 dB) in the 8-11.5 GHz range. Possible fabrication problems include the conductivity problems at certain parts of the antenna surfaces and the smoothness problems in some portions of the surfaces.

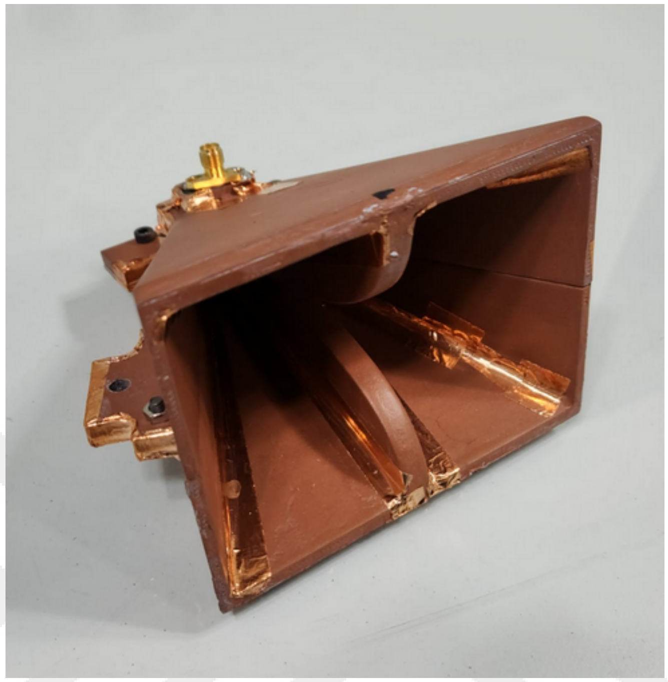

Figure 3.22: Fabricated double ridge horn antenna.

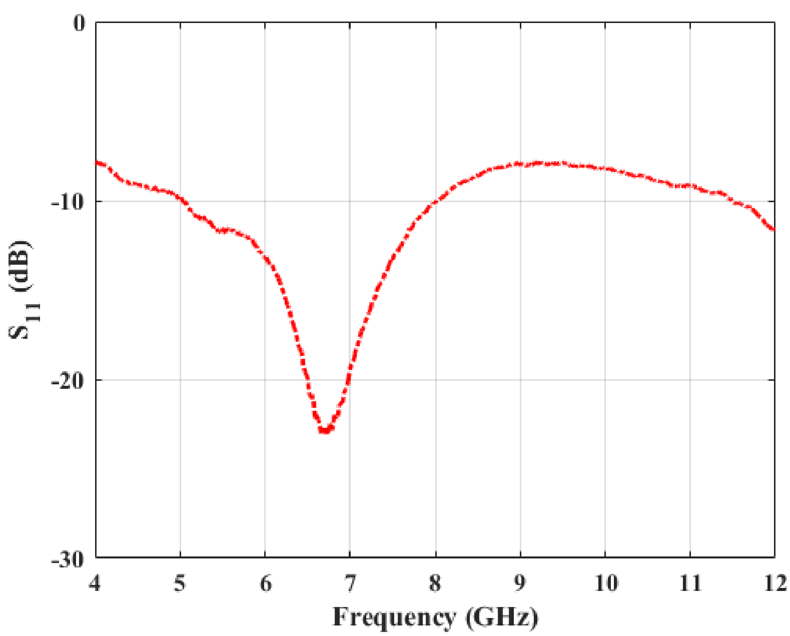

Figure 3.23: Measured S_{11} spectrum of the double ridge horn antenna.

Chapter 4

Absorber Performance Measurements

This chapter starts with describing the waveguide measurements, in which the electrical properties of the materials, such as permittivity and loss tangent, are measured across the 8.2-12.4 GHz frequency range. The materials that satisfy the desired permittivity values are used as the dielectric in the absorber fabrication. Next, the design and fabrication of a free-space measurement setup to measure the absorption response of the fabricated absorbers under different oblique incidence angles are provided. The measurement results of the fabricated absorbers are compared with those of the simulations. Lastly, optical transmittance measurements of the fabricated absorbers for visible wavelengths using optical spectrophotometer are presented.

4.1 X-band Waveguide Measurements

The waveguide measurement can be considered as a non-resonant method that allows general knowledge of electrical properties of materials in a wide frequency range [65]. Figure 4.1 shows our waveguide setup working at the X-band (8.2-12.4 GHz). The setup has a sample holder that is located between the standard section of the waveguide and the coaxial to waveguide transition piece in order to easily place the material under test. This holder allows the material under test to be placed vertically without unsettling waveguide pieces each time. Two coaxial cables were connected between the coaxial to waveguide transition piece and the vector network analyzer (VNA) for both transmission and reflection coefficients to be measured.

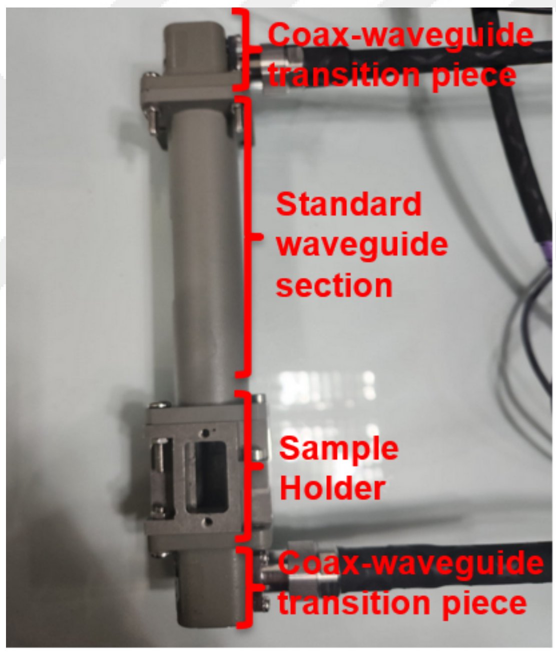

Figure 4.1: X-band waveguide measurement setup.

Before starting the measurement, we first calibrated the system with TRL (thru-reflect-line) calibration that is the most suitable calibration technique in terms of accuracy for high performance and minimal standard definition for waveguide setups [66]. Thru standard is a zero-length line and two ports are directly connected. Reflect standard stands for highly reflective metal piece for connecting the ports separately. Lastly, the line standard has a non-zero length piece to be connected between two ports [67]. During the entire calibration process, we fixed the standard section of waveguide and the sample holder for one side of the coaxial to waveguide piece. The calibration was performed as follows: 1) We selected the thru standard and connected two ports directly.

2) We joined the reflect standard, which is a metal plate, to the ports separately.
3) We used a $\lambda/4$ length shim between two ports to represent the line standard.
4) After finishing the calibration, we saved the calibration data into the memory of the VNA.

In this thesis, we showed measurement results for the electrical properties of glass, PMMA, and polytetrafluoroethylene (PTFE) as examples. To fit these materials into the waveguide, we used a CO_2 laser source machine for cutting the PMMA, and a dicing saw for the Glass pieces. On the other hand, the PTFE sample was prepared by using the CNC cutting machine available at UNAM. All pieces have dimensions of 10.16 mm in width and 22.15 in length with various thicknesses.

After placing the material into the sample holder, we opened Keysight material measurement suite. First, we selected a defined measurement option and chose the desired frequency band as the X-band. After the frequency band selection, VNA parameters were assigned automatically from the software, as shown in Figure 4.2.

One of the most crucial points of waveguide measurements is to decide which measurement model is best suited to calculate the electrical properties of materials from the transmission and reflection coefficients. In the measurement model section, several algorithms are provided in the software. One of them is the well-known Nicholson and Ross algorithm [68]. However, this algorithm yields ambiguous results when the thickness of materials to be tested is an integer multiple of half wavelength, and provides inaccurate data when these materials have a low loss [69]. Because of these drawbacks, we used a modified version of Nicholson and Ross algorithm that is provided in the software, namely the polynomial fit transmission ω model algorithm. This is based on a functional relationship between the material properties and the frequency. This functional relationship is modeled as an n^{th} order polynomial and by using an iterative technique to fit the measured S-parameters to a polynomial that is derived from the material properties, possible errors due to the noise and imperfect calibration are reduced

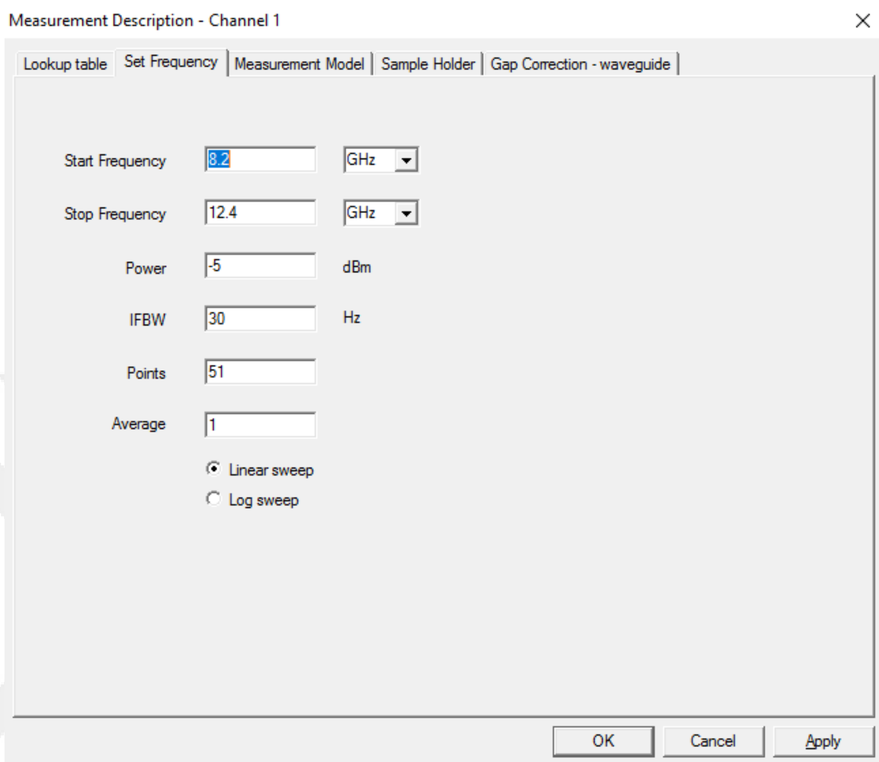

Figure 4.2: VNA measurement properties.

[70]. The algorithm can be used for long, low-loss, and non-magnetic materials and provide significantly improved results than the Nicholson-Ross algorithm [71]. The algorithm description is shown in Figure 4.3. We used this algorithm for calculating the electrical permittivity and loss tangent of PMMA, glass, and PTFE samples.

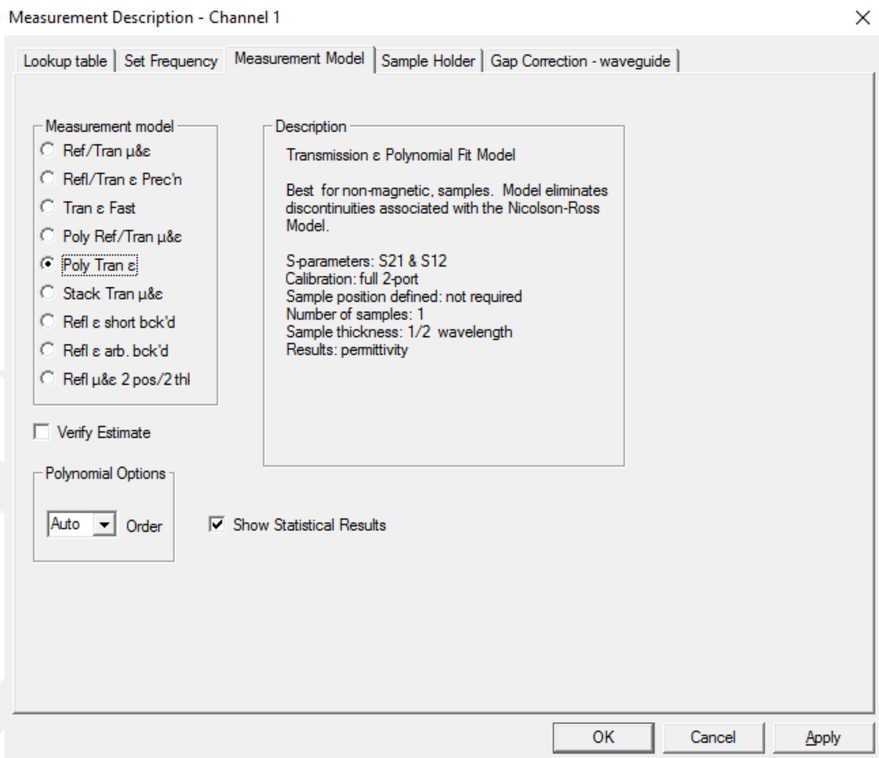

Figure 4.3: Polynomial fit algorithm description.

Lastly, the sample holder properties must be decided as shown in Figure 4.4. The software automatically fills the sample holder type as a waveguide and its cut-off frequency. We measured the sample holder length as 40 mm. Distance to the sample and the sample thickness parameters vary based on which material is used and where it is placed in the sample holder. We used a caliper to measure these two parameters for each material.

After these steps, we measured the S-parameters by clicking the trigger measurement button in the software. Then, the software calculated permittivity, permeability, and the electric and magnetic losses from these measured S-parameters. For PMMA, glass, and PTFE, relative permittivity and tangent loss graphs can be found in Figure 4.5, Figure 4.6, and Figure 4.7, respectively. For PMMA, under room temperature, relative permittivity is reported between 2.58-2.64 at 11 GHz in [72]. Figure 4.5 provides a close estimation of the relative permittivity of PMMA given in the literature. For the glass case, a glass disk is measured at 9.2 GHz with a 0.3 percent error and the relative permittivity is reported to

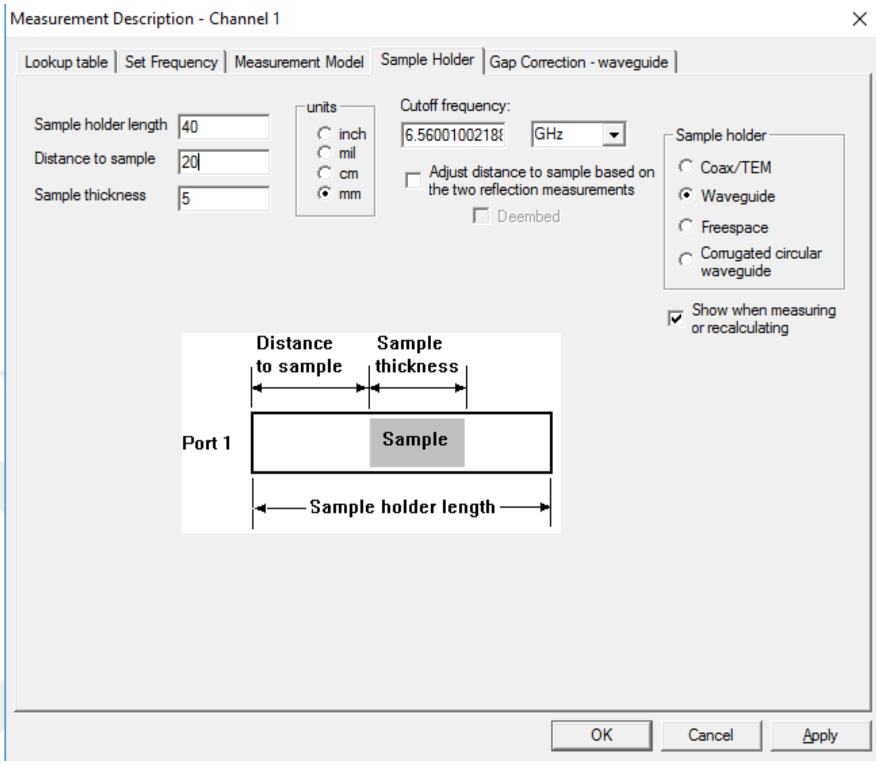

Figure 4.4: Sample holder dimensions option.

be 6.15 in [73]. A similar result is obtained as shown in Figure 4.6. Lastly, the relative permittivity of PTFE is reported to be 2.1 for the X-band frequencies in [74]. However, our measurements showed that PTFE's relative permittivity is around 3.0. The difference between our measurements and the literature can be related to the material's chemical properties such as different composites used along the material itself [75].

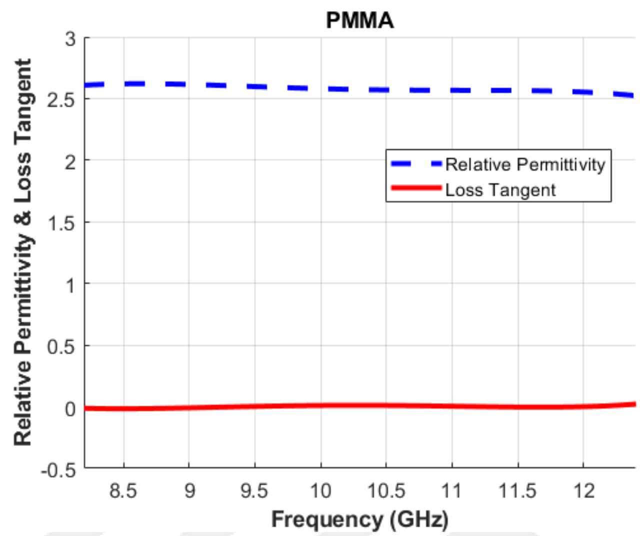

Figure 4.5: Measured relative permittivity and loss tangent of PMMA.

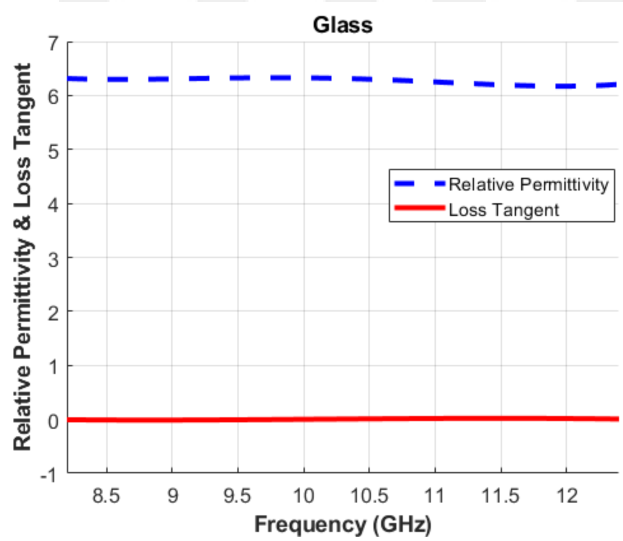

Figure 4.6: Measured relative permittivity and loss tangent of glass.

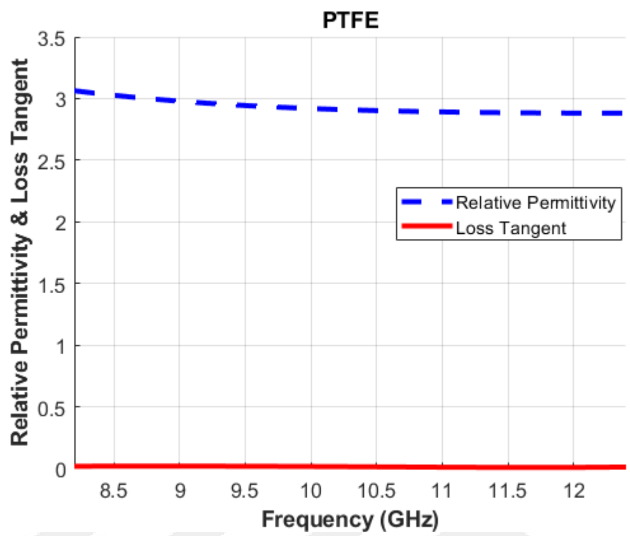

Figure 4.7: Measured relative permittivity and loss tangent of PTFE.

4.2 Free-Space Measurements

To test the fabricated absorbers under normal and oblique incidence angles, we conducted free-space absorption measurements. During the free-space measurements, we recorded only the reflection coefficients since the transmission values of the absorbers are neglected due to the ITO ground plane. Additionally, we measured both TE and TM polarizations.

There are several important details that have to be taken into consideration in free-space absorber measurements. First, the absorber must be in the far zone of the antennas. Starting with the $2D^2/\lambda$ formula, where $D = 12.2$ cm is the largest dimension of our double ridge horn antenna, as illustrated in Figure 4.8, the far-field distance is found to be 120 cm at 12 GHz. We calculated the far-field distance for 12 GHz because our designed absorber needs to be measured up to 12 GHz. During the measurements, we set the distance (r) between the absorber and the antenna to approximately 130 cm. Note that 130 cm distance also satisfies both $r > \lambda$ and $r > D$ conditions.

The second important aspect is the need of a conducting reference plane for

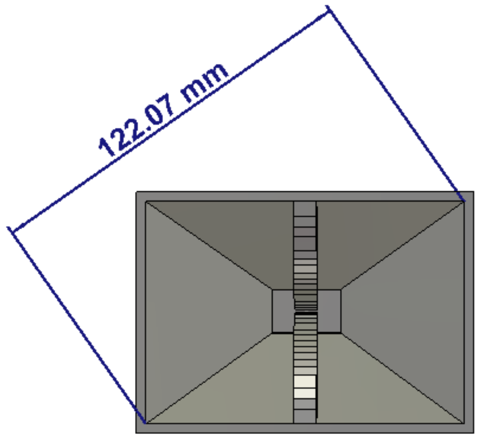

Figure 4.8: Largest aperture dimension (i.e., D) of the double ridge horn antenna.

normalization purposes. Therefore, an aluminum metal plate with the same width and height values as those of the absorber under test was cut in a horizontal band saw machine as shown in Figure 4.9. We used this metal plate to normalize the S-parameters coming from the absorbers. The formula provided in [76] was used to calculate the S-parameters of the absorber:

$$S_{11,absorber-calibrated}(\omega) = \frac{S_{11,absorber}(\omega) - S_{11,air}(\omega)}{S_{11,metal}(\omega) - S_{11,air}(\omega)} \tag{4.1}$$

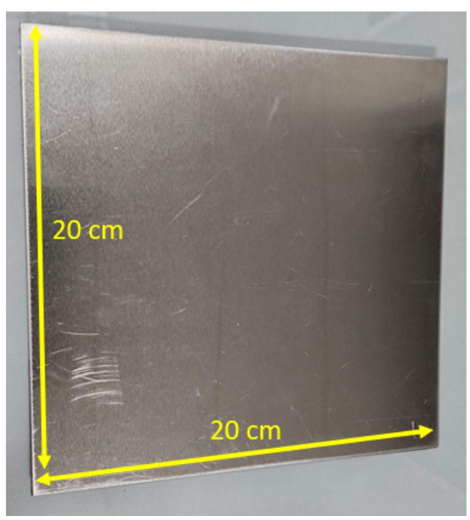

Figure 4.9: An aluminum metal plate used for normalization purposes in the measurements.

The third issue is to be able to remove the undesired effects coming from the cables and connectors during the measurements. Hence, we performed one-port calibration for the desired frequency ranges. After the calibration, cable positions were not changed. Furthermore, several commercial dielectric absorbers were placed at all critical places to minimize the environmental effects (clutter reflections) since they can achieve -17 dB reflectivity in the frequency range of 0.6-20 GHz [77].

Finally, it should be noted that, because the measurements were repeated many times for both TE and TM polarizations, we decided to rotate the absorber under test 90° around its centered axis without changing the position translationally.

We used only one antenna for the normal incidence measurements and the 2D view of the setup is sketched in Figure 4.10. We placed the absorber under test vertically and stabilized it using 3D-printed pieces on the optical table. Furthermore, we fixed the antenna to the optical table using optical table components and arranged its height so that the antenna points to the absorber's center. A picture of the prepared setup is shown in Figure 4.11.

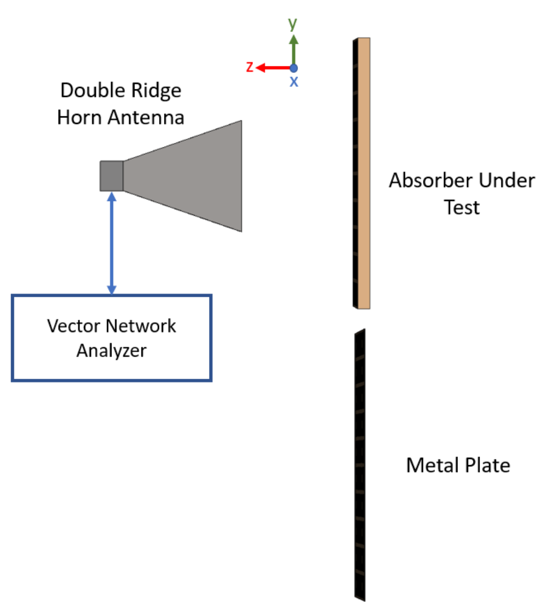

Figure 4.10: 2D view of normal incidence measurement setup.

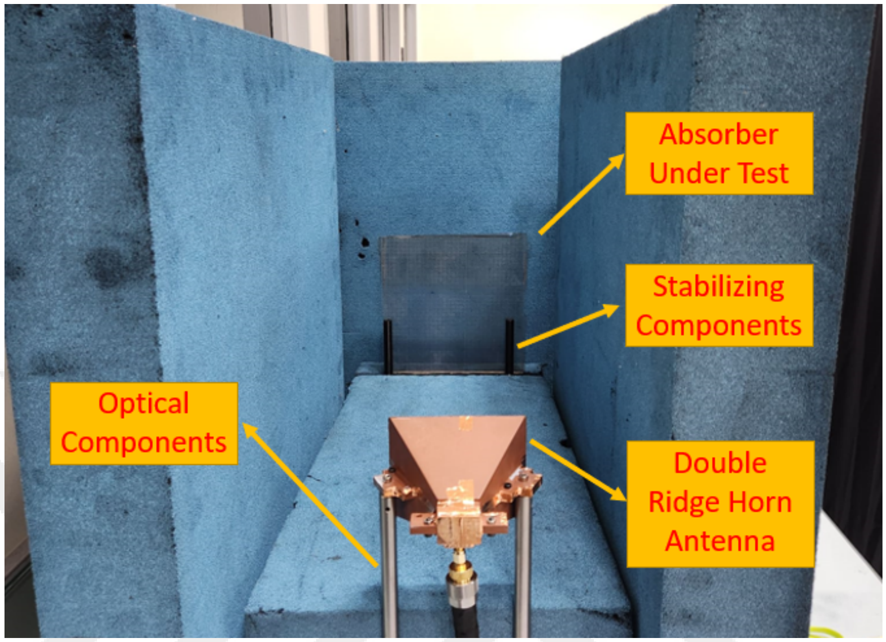

Figure 4.11: Normal incidence experimental setup.

We measured the normal incidence absorption and the measurement results are presented in Figure 4.12 together with simulation results. As can be seen from Figure 4.12, there is a good agreement between the simulated and the measured absorption spectra.

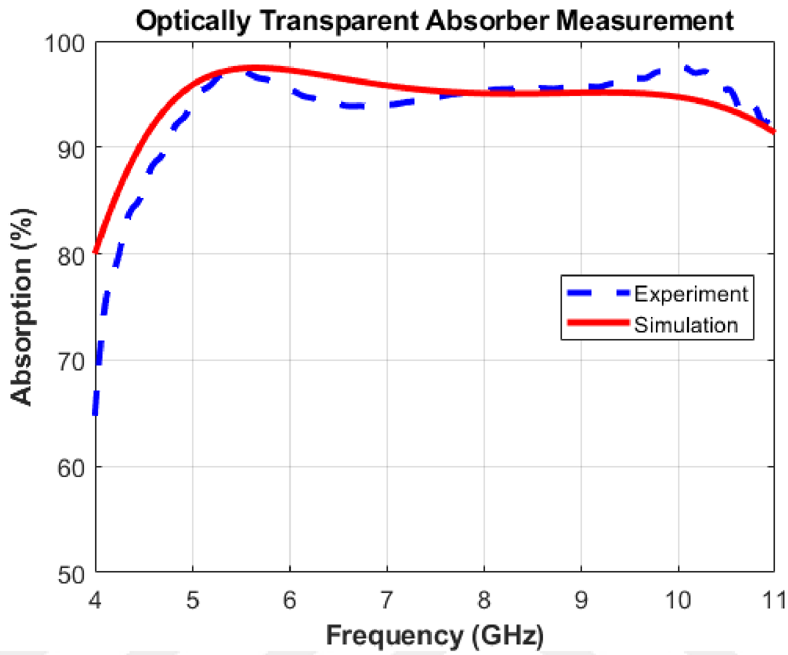

Figure 4.12: Experimentally measured and numerically simulated absorption spectra of our optically transparent absorber under normal incidence.

In the case of the oblique incidence, we used two antennas, as illustrated in Figure 4.13, which describes the oblique incidence measurement setup. There are two possibilities for positioning the antennas and the absorber while performing the oblique incidence measurements. The first possibility is to move both antennas while fixing the absorber's position. The second possibility is to fix one antenna and move the other antenna while rotating the absorber around its center line. In our experimental setup, we adopted the second possibility since moving two antennas simultaneously results in positioning errors and operating the setup becomes more complicated.

To determine the antenna and absorber positions correctly, we placed two antennas and the absorber in the same line as shown in Figure 4.14. Then, we changed one antenna's position and rotated the absorber around its center line for different oblique incidence angles, as illustrated in Figure 4.15 for $\theta = 45°$ incidence. Then, by considering Snell's law of reflection, we moved the moving antenna by 90° along the arch at fixed radial distance $r = 130$ cm. The reason behind changing the antenna's angle twice the absorber's rotation angle is due to

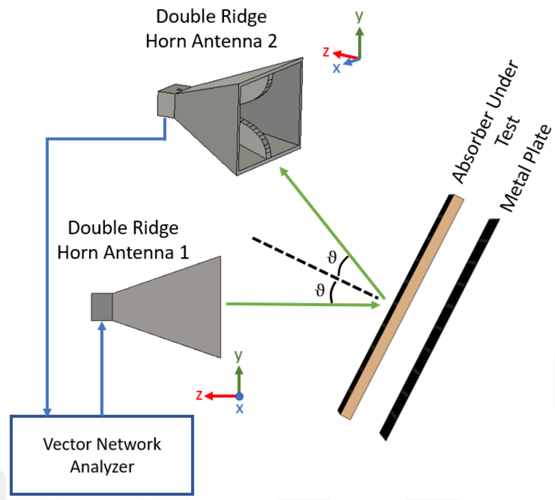

Figure 4.13: 2D view of oblique incidence measurement setup.

the fixed position of the other antenna. Furthermore, both antennas were lined up in such a way that they always directed to the center of the absorber.

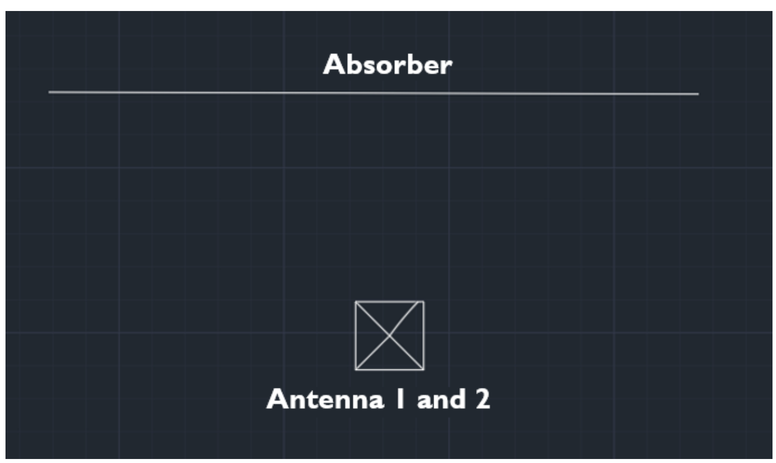

Figure 4.14: Initial positions of the absorber and the antennas.

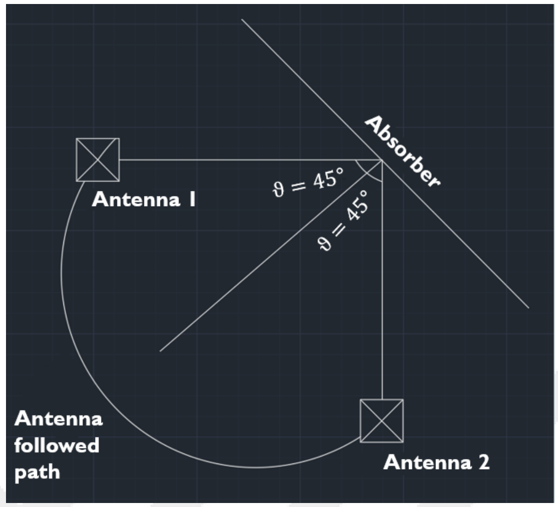

Figure 4.15: Antennas and absorber positions for $\theta = 45°$ oblique incidence angle.

Concerning the preparation of the measurement system, we built a rotational stage by using a step motor, a power supply, and a microcontroller to rotate the absorber accurately. We also fabricated holders for both antennas and the absorber. Moreover, we added a laser marking system to determine the position of the moving antenna continuously, as well as for alignment purposes.

In rotational stage design, we used a Nema 23 step motor. We connected this step motor to the TB6600 motor driver, which allows the step motor to run at different micro-step resolutions. For instance, 200 to 6400 steps can be chosen to turn the absorber 360° in a single run. The step motor was connected to the Arduino microcontroller, and the desired voltage and current values were provided to the components with a power supply. All the components were placed in a holder box.

The absorber holder that helps to rotate the absorber with the step motor consists of a plate on which the absorber can be placed vertically and an apparatus to compress the absorber from its backside, as shown in Figure 4.16. Screws and nuts can tighten this apparatus. We attached the sample holder with a bearing to the shaft of the step motor. Additionally, we placed three wheels upside-down on the holder box to increase the mechanical stability. When the sample holder was rotating, these wheels also rotate and any possibility of falling or making unstable movements was eliminated. The entire setup is shown in Figure 4.17.

Figure 4.16: Absorber under test, absorber holder (orange) and apparatus (black).

We used the step motor to determine the position of the moving antenna. Briefly, we placed a laser source under the stationary antenna, which is illustrated in Figure 4.18. This laser source points directly toward the mirror, which we placed on the absorber holder aligned with the center line of the absorber. After rotating the absorber by the desired angle, the laser reflects from the mirror and marks the position of the moving antenna. The entire system is given in Figure 4.19.

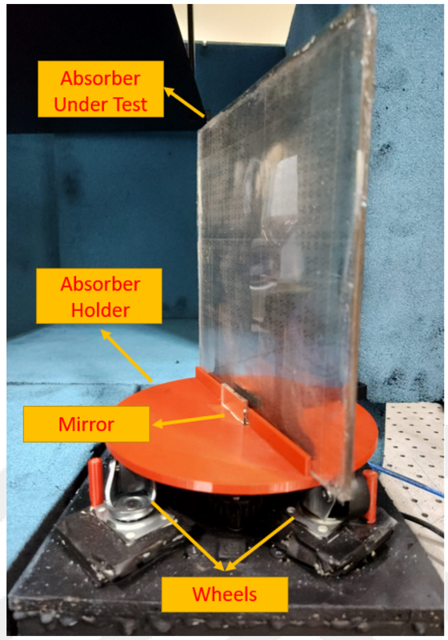

Figure 4.17: Absorber and its holder placed on the holder box.

Finally, we prepared a simple graphical user interface (GUI) to control the entire system. In this program, the user can write the desired angle of rotation into the box and by clicking the apply button, the system rotates in the clockwise direction, and by clicking the reset button, the system rotates in the counter-clockwise direction. The output result section of GUI shows if the rotation is successful or not.

Apart from controlling the rotations, this GUI program also controls the VNA. In operation, first, the instrument connection status button must be clicked. Underneath this button, status of the connection between the computer and VNA is displayed. If the connection is successful, we can take data from VNA directly by clicking the start metal and absorber measurement buttons. Figure 4.20 shows this GUI of our measurement system.

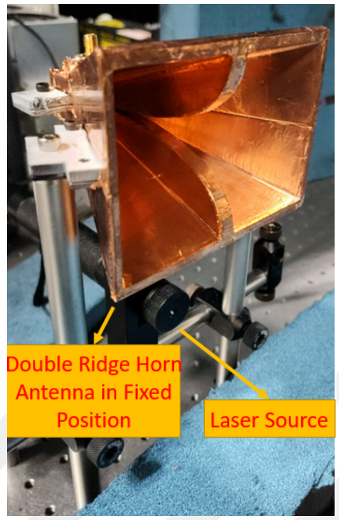

Figure 4.18: Placement of the laser source under the stationary antenna.

Using this described setup, we measured the performance of our optically transparent metamaterial absorber under different oblique angles of incidence. The simulation and measurement results are provided in pairs for systematically varied incident angles for comparison in Figure 4.21 and Figure 4.22 using TE and TM polarizations, respectively. The results show that the numerically simulated and experimentally measured absorption spectra agree well with each other.

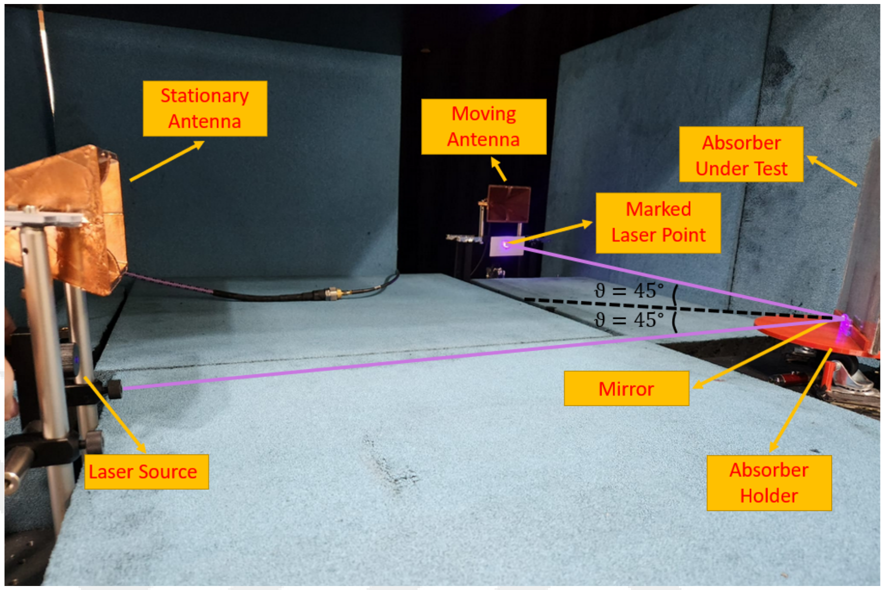

Figure 4.19: Complete oblique incidence measurement setup.

4.3 Optical Measurements

We fabricated a 3cm-by-3cm piece of the same optically transparent absorber using the identical structure following the identical fabrication steps, as shown in Figure 4.23, in order to measure its optical transmission. The reason for fabricating a small absorber is to place it inside the Cary 60 UV-Vis spectrophotometer.

The results of the optical transmission measurements are presented in Figure 4.25. Since we bonded transparent materials as ITO and PMMA with transparent glue, we achieved 65% average transmission in visible wavelengths. To further demonstrate the optical transparency, we put the optically transparent absorber on a piece of paper with a Bilkent University logo. As seen in Figure 4.26, the writings underneath the absorber can be clearly read.

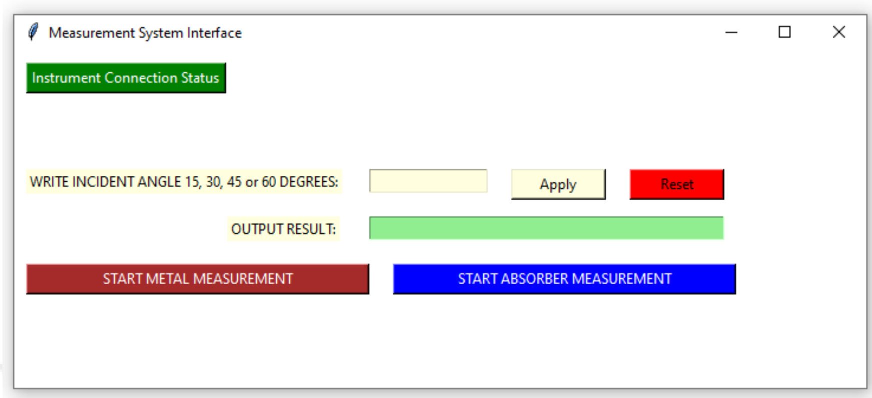

Figure 4.20: Graphical user interface of our measurement system.

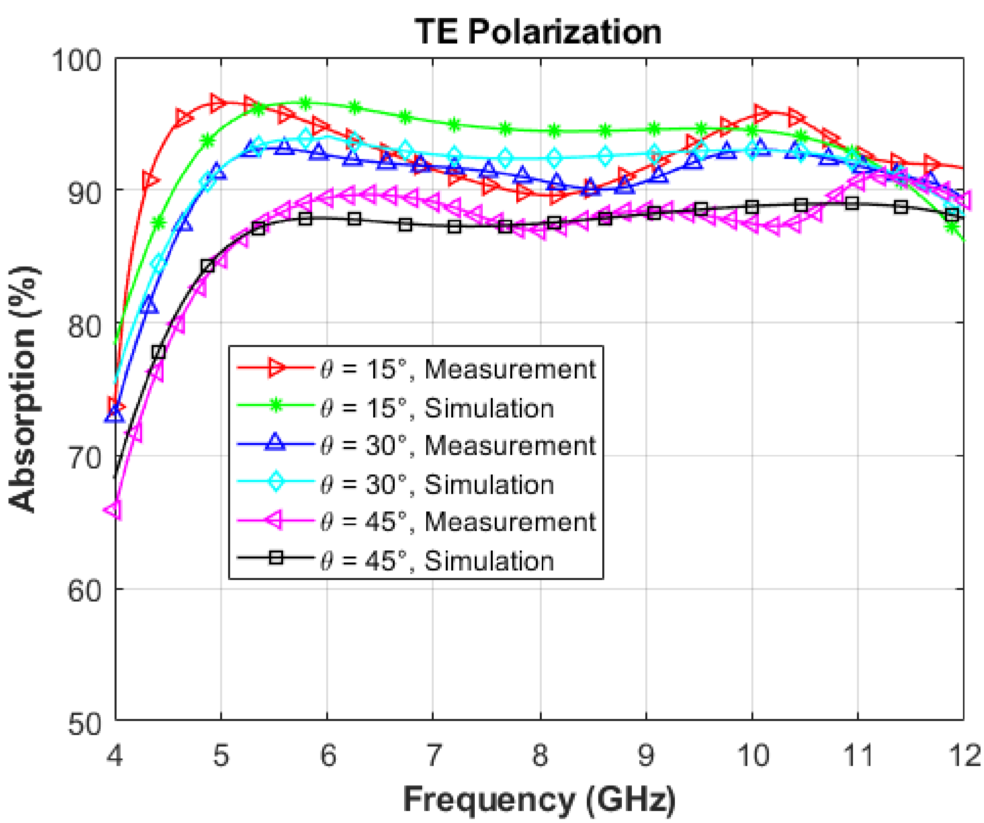

Figure 4.21: Oblique incidence absorption measurement results of our optically transparent absorber under TE polarization, along with the simulation results.

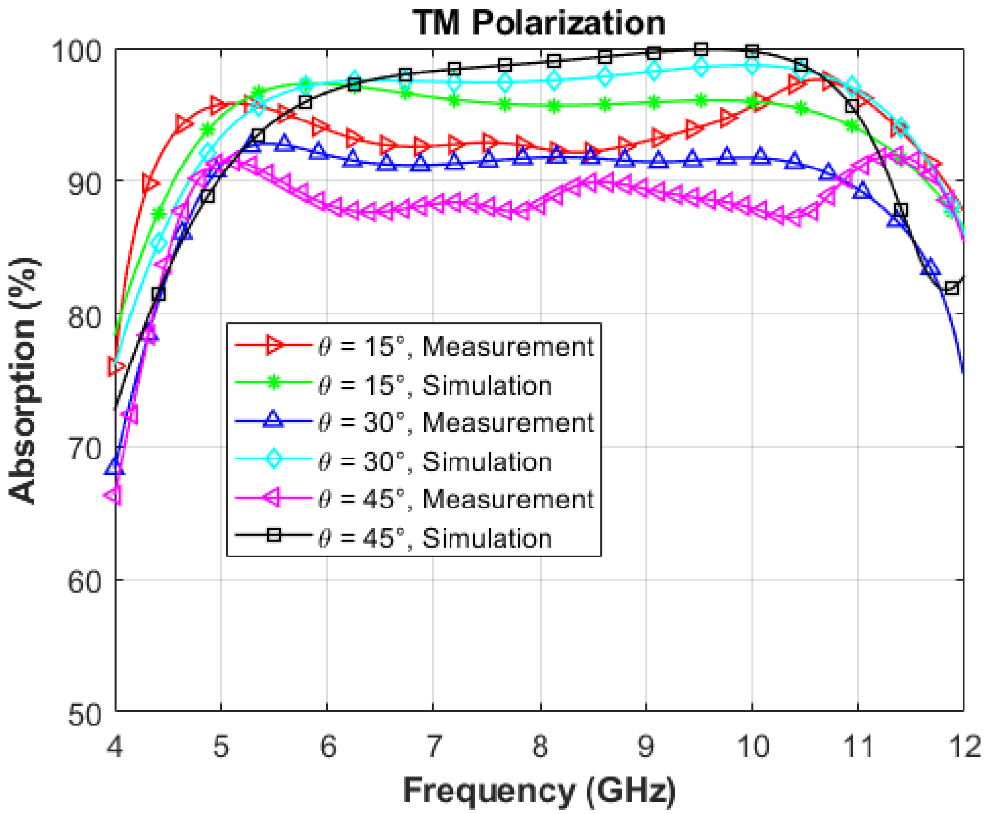

Figure 4.22: Oblique incidence absorption measurement results of our optically transparent absorber under TM polarization, along with the simulation results.

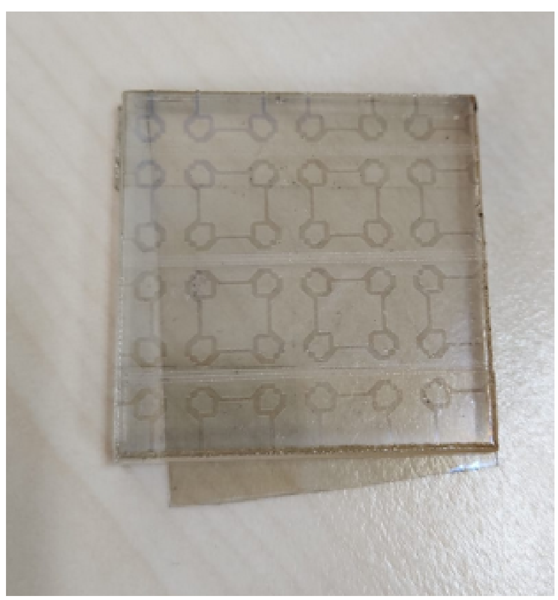

Figure 4.23: Optically transparent absorber sample.

Figure 4.24: Sample placed inside Cary UV-Vis spectrophotometer.

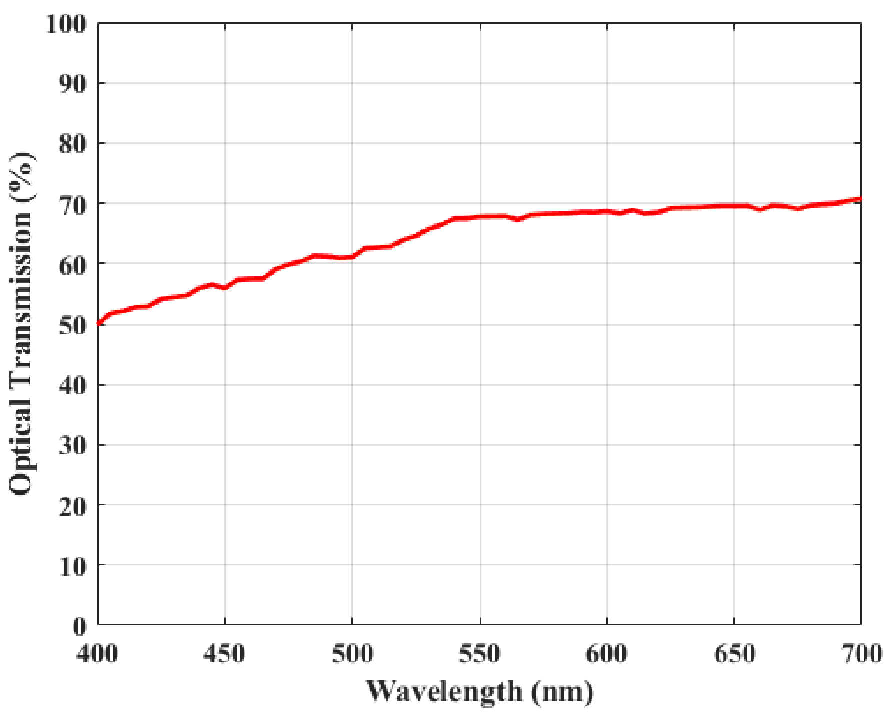

Figure 4.25: Measured optical transmission of our fabricated absorber in the visible.

Figure 4.26: Optically transparent absorber placed above Bilkent University logo that can be clearly seen through.

Chapter 5

Conclusion and Future Outlook

5.1 Conclusion

In this thesis, we developed and demonstrated a single-layer optically transparent RF absorber that we designed and built to impart a unique set of essential properties including the broadband absorption, the low structural thickness, the polarization insensitiveness, the performance robustness for different oblique incidence angles in microwave regime as well as the high optical transparency in the visible. The initial absorber design was based on a single square loop shape, which was further modified by introducing four small square loops in the corners of the starting loop and optimizing the dimensions using particle swarm optimization. As CST Microwave Studio simulations show, the proposed final absorber can achieve above 90% absorption between 4.4-11.2 GHz and more than 95% between 4.9-9.9 GHz for all polarization angles. Furthermore, over 90% absorption is preserved up to 60° for TM and up to 40° for TE polarizations. Lastly, a specific fabrication process was developed for the absorber prototypes.

In order to test the fabricated absorbers, three types of antennas as Vivaldi, X-band standard horn, and double ridge horn antennas, were designed, simulated, and fabricated. Vivaldi and double ridge horn antennas satisfied less than

-10 dB $|S_{11}|$ between 4-12 GHz and X-band horn antenna satisfied -10 dB $|S_{11}|$ between 8-12 GHz. In the measurements section, an X-band waveguide was used to measure the electrical properties of the dielectric materials that can be used in the fabrication of the absorbers. The relative permittivity and loss tangent of the PMMA, glass and PTFE samples were found close to values reported in the literature. Then, a measurement setup was designed and built by using fabricated antennas, holders and electronic components to characterize RF absorption. The experimentally measured absorption spectra results agree fairly well with those simulated ones. Furthermore, optical transmittance in the visible range was measured by using a spectrophotometer, and 65% average transmittance was recorded for the fabricated prototype.

The findings of this thesis indicated that the proposed and validated optically transparent RF absorber hold great promise for use in stealth window applications.

5.2 Future Outlook

As our future research work, we apply machine learning techniques to design such RF absorbers. As explained in the design and simulation discussions of our optically transparent absorbers, the Matlab to CST interface was used to create random pixel data and create absorber designs. The simulations of these designs in CST give the S-parameters and electric field monitor results. We may use these data to train and validate the networks. Simply, a design matrix that consists of 1's and 0's can be used as the input data for training purposes, and S-parameters and near-field electric field results as the output data. After the training process, this model should be able to predict near-field electric field values and absorption results of the designs. Such a visual comparison between the simulated and predicted near-field electric field data is given in Figure 5.1 as for preliminary work.

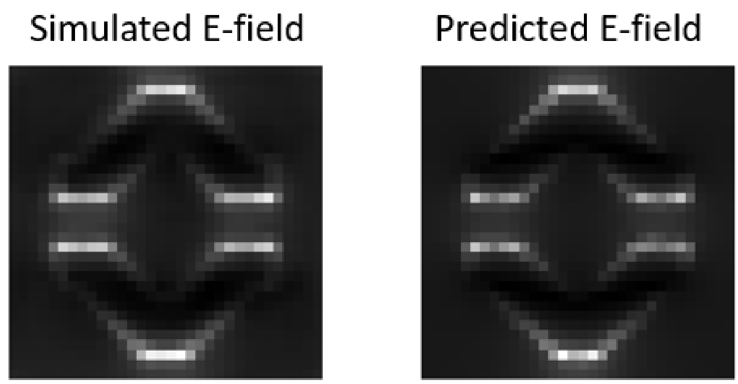

Figure 5.1: Simulated and predicted results of near-field electric field.

Bibliography

[1] W. Li, M. Xu, H. Xu, X. Wang, and W. Huang, "Metamaterial absorbers: From tunable surface to structural transformation,"Advanced Materials, vol. 34, no. 38, p. 2202509, 2022.

[2] H. Mei et al., "Metamaterial absorbers towards broadband, polarization insensitivity and tunability,"Optics & Laser Technology, vol. 147, p. 107627, 2022.

[3] T. Wanghuang, W. Chen, Y. Huang, and G. Wen, "Analysis of metamaterial absorber in normal and oblique incidence by using interference theory," AIP Advances, vol. 3, no. 10, p. 102118, 2013.

[4] X. Liu, F. Xia, M. Wang, J. Liang, and M. Yun, "Working Mechanism and progress of electromagnetic metamaterial perfect absorber," Photonics, vol. 10, no. 2, p. 205, 2023.

[5] X. Zeng, M. Gao, L. Zhang, G. Wan, and B. Hu, "Design of a triple-band metamaterial absorber using equivalent circuit model and interference theory," Microwave and Optical Technology Letters, vol. 60, no. 7, pp. 1676–1681, 2018.

[6] H.-T. Chen, "Interference theory of metamaterial perfect absorbers," Optics Express, vol. 20, no. 7, p. 7165, 2012.

[7] K. Ling et al., "Microfluidic tunable inkjet-printed metamaterial absorber on paper," Optics Express, vol. 23, no. 1, p. 110, 2015.

[8] E. Erdem and A. H. Yuzer, "Textile-based 3D Metamaterial Absorber Design for X-band application," Waves in Random and Complex Media, pp. 1–10, 2022.

[9] S. Tian et al., "Transparent broadband wide-angle polarization-insensitive metasurface absorber for microwave antireflection," 2019 IEEE MTT-S International Wireless Symposium (IWS), 2019.

[10] M. Bakir et al., "Sensory applications of resonator based metamaterial absorber," Optik, vol. 168, pp. 741–746, 2018.

[11] M. A. Shukoor, S. Dey, and S. K. Koul, "A simple polarization-insensitive and wide angular stable circular ring based UNDECA-band absorber for EMI/EMC applications," IEEE Transactions on Electromagnetic Compatibility, vol. 63, no. 4, pp. 1025–1034, 2021.

[12] P. Min, Z. Song, L. Yang, V. G. Ralchenko, and J. Zhu, "Optically transparent flexible broadband metamaterial absorber based on topology optimization design," Micromachines, vol. 12, no. 11, p. 1419, 2021.

[13] C. Zhang, Q. Cheng, J. Yang, J. Zhao, and T. J. Cui, "Broadband metamaterial for optical transparency and microwave absorption," Applied Physics Letters, vol. 110, no. 14, p. 143511, 2017.

[14] S. Li et al., "Ultrathin optically transparent metamaterial absorber for broadband microwave invisibility of Solar Panels," Journal of Physics D: Applied Physics, vol. 55, no. 4, p. 045101, 2021.

[15] T. Jang, H. Youn, Y. J. Shin, and L. J. Guo, "Transparent and flexible polarization-independent microwave broadband absorber," ACS Photonics, vol. 1, no. 3, pp. 279–284, 2014.

[16] R. Deng, K. Zhang, M. Li, L. Song, and T. Zhang, "Targeted design, analysis and experimental characterization of flexible microwave absorber for window application," Materials & Design, vol. 162, pp. 119–129, 2019.

[17] Z. Meng et al., "Multi-spectral functional metasurface simultaneously with visible transparency, low infrared emissivity and wideband microwave absorption," Infrared Physics & Technology, vol. 110, p. 103469, 2020.

[18] P. Garg and P. Jain, "A review of metamaterial absorbers and their application in sensors and Radar Cross-Section Reduction," Microwave and Optical Technology Letters, vol. 65, no. 2, pp. 387–411, 2022.

[19] H. Xiong, J.-S. Hong, C.-M. Luo, and L.-L. Zhong, "An ultrathin and broadband metamaterial absorber using multi-layer structures," Journal of Applied Physics, vol. 114, no. 6, p. 064109, 2013.

[20] L. Li and Z. Lv, "Ultra-wideband polarization-insensitive and wide-angle thin absorber based on resistive metasurfaces with three resonant modes," Journal of Applied Physics, vol. 122, no. 5, p. 055104, 2017.

[21] H. Luo, Y. Z. Cheng, and R. Z. Gong, "Numerical Study of metamaterial absorber and extending absorbance bandwidth based on multi-square patches," The European Physical Journal B, vol. 81, no. 4, pp. 387–392, 2011.

[22] L. Li et al., "A band enhanced metamaterial absorber based on E-shaped all-dielectric resonators," AIP Advances, vol. 5, no. 1, p. 017147, 2015.

[23] S. Li et al., "Wideband, thin, and polarization-insensitive perfect absorber based the double octagonal rings metamaterials and lumped resistances," Journal of Applied Physics, vol. 116, no. 4, p. 043710, 2014.

[24] P. Munaga, S. Ghosh, S. Bhattacharyya, and K. V. Srivastava, "A fractal-based compact broadband polarization insensitive metamaterial absorber using lumped resistors," Microwave and Optical Technology Letters, vol. 58, no. 2, pp. 343–347, 2015.

[25] S. Fan and Y. Song, "Bandwidth-enhanced polarization-insensitive metamaterial absorber based on fractal structures," Journal of Applied Physics, vol. 123, no. 8, p. 085110, 2018.

[26] S. Ghosh, S. Bhattacharyya, Y. Kaiprath, and K. Vaibhav Srivastava, "Bandwidth-enhanced polarization-insensitive microwave metamaterial absorber and its equivalent circuit model," Journal of Applied Physics, vol. 115, no. 10, p. 104503, 2014.

[27] Q. Huang et al., "Metamaterial electromagnetic wave absorbers and devices: Design and 3D microarchitecture," Journal of Materials Science & Technology, vol. 108, pp. 90–101, 2022.

[28] B. A. Munk, P. Munk, and J. Pryor, "On designing Jaumann and circuit analog absorbers (ca absorbers) for oblique angle of incidence," IEEE Transactions on Antennas and Propagation, vol. 55, no. 1, pp. 186–193, 2007.

[29] J. Chen, Y. Shang, and C. Liao, "Double-layer circuit analog absorbers based on resistor-loaded square-loop arrays," IEEE Antennas and Wireless Propagation Letters, vol. 17, no. 4, pp. 591–595, 2018.

[30] D. Kundu, A. Mohan, and A. Chakrabarty, "Single-layer wideband microwave absorber using array of crossed dipoles," IEEE Antennas and Wireless Propagation Letters, vol. 15, pp. 1589–1592, 2016.

[31] S.-J. Li et al., "Analysis and design of three-layer perfect metamaterial-inspired absorber based on double split-serration-rings structure," IEEE Transactions on Antennas and Propagation, vol. 63, no. 11, pp. 5155–5160, 2015.

[32] P. Ranjan, A. Choubey, S. K. Mahto, and R. Sinha, "A six-band ultra-thin polarization-insensitive pixelated metamaterial absorber using a novel binary wind driven optimization algorithm," Journal of Electromagnetic Waves and Applications, vol. 32, no. 18, pp. 2367–2385, 2018.

[33] A. Dimitriadis, N. Kantartzis, and T. Tsiboukis, "A polarization-/angle-insensitive, bandwidth-optimized, metamaterial absorber in the microwave regime," Applied Physics A, vol. 109, no. 4, pp. 1065–1070, 2012.

[34] B. Bian et al., "Novel triple-band polarization-insensitive wide-angle ultra-thin microwave metamaterial absorber," Journal of Applied Physics, vol. 114, no. 19, p. 194511, 2013.

[26] S. Ghosh, S. Bhattacharyya, Y. Kaiprath, and K. Vaibhav Srivastava, "Bandwidth-enhanced polarization-insensitive microwave metamaterial absorber and its equivalent circuit model," Journal of Applied Physics, vol. 115, no. 10, p. 104503, 2014.

[27] Q. Huang et al., "Metamaterial electromagnetic wave absorbers and devices: Design and 3D microarchitecture," Journal of Materials Science & Technology, vol. 108, pp. 90–101, 2022.

[28] B. A. Munk, P. Munk, and J. Pryor, "On designing Jaumann and circuit analog absorbers (ca absorbers) for oblique angle of incidence," IEEE Transactions on Antennas and Propagation, vol. 55, no. 1, pp. 186–193, 2007.

[29] J. Chen, Y. Shang, and C. Liao, "Double-layer circuit analog absorbers based on resistor-loaded square-loop arrays," IEEE Antennas and Wireless Propagation Letters, vol. 17, no. 4, pp. 591–595, 2018.

[30] D. Kundu, A. Mohan, and A. Chakrabarty, "Single-layer wideband microwave absorber using array of crossed dipoles," IEEE Antennas and Wireless Propagation Letters, vol. 15, pp. 1589–1592, 2016.

[31] S.-J. Li et al., "Analysis and design of three-layer perfect metamaterial-inspired absorber based on double split-serration-rings structure," IEEE Transactions on Antennas and Propagation, vol. 63, no. 11, pp. 5155–5160, 2015.

[32] P. Ranjan, A. Choubey, S. K. Mahto, and R. Sinha, "A six-band ultra-thin polarization-insensitive pixelated metamaterial absorber using a novel binary wind driven optimization algorithm," Journal of Electromagnetic Waves and Applications, vol. 32, no. 18, pp. 2367–2385, 2018.

[33] A. Dimitriadis, N. Kantartzis, and T. Tsiboukis, "A polarization-/angle-insensitive, bandwidth-optimized, metamaterial absorber in the microwave regime," Applied Physics A, vol. 109, no. 4, pp. 1065–1070, 2012.

[34] B. Bian et al., "Novel triple-band polarization-insensitive wide-angle ultra-thin microwave metamaterial absorber," Journal of Applied Physics, vol. 114, no. 19, p. 194511, 2013.

[35] A. Bhardwaj, G. Singh, K. V. Srivastava, J. Ramkumar, and S. A. Ramakrishna, "Polarization-insensitive optically transparent microwave metamaterial absorber using a complementary layer," IEEE Antennas and Wireless Propagation Letters, vol. 21, no. 1, pp. 163–167, 2022.

[36] H. Jiang et al., "A conformal metamaterial-based optically transparent microwave absorber with high angular stability," IEEE Antennas and Wireless Propagation Letters, vol. 20, no. 8, pp. 1399–1403, 2021.

[37] F. Costa, A. Monorchio, and G. Manara, "Analysis and design of Ultra thin electromagnetic absorbers comprising resistively loaded high impedance surfaces," IEEE Transactions on Antennas and Propagation, vol. 58, no. 5, pp. 1551–1558, 2010.

[38] M. I. Hossain, N. Nguyen-Trong, K. H. Sayidmarie, and A. M. Abbosh, "Equivalent circuit design method for wideband nonmagnetic absorbers at low microwave frequencies," IEEE Transactions on Antennas and Propagation, vol. 68, no. 12, pp. 8215–8220, 2020.

[39] D. Kundu, A. Mohan, and A. Chakraborty, "Ultrathin polarization independent absorber with enhanced bandwidth by incorporating Giusepe Peano fractal in square ring," Microwave and Optical Technology Letters, vol. 57, no. 5, pp. 1072–1078, 2015.

[40] J. Kennedy and R. Eberhart, "Particle swarm optimization," Proceedings of ICNN'95 - International Conference on Neural Networks.

[41] A. L. Pereira de Siqueira Campos, R. H. Maniçoba, and A. G. d'Assunção, "Investigation of enhancement band using double screen frequency selective surfaces with Koch fractal geometry at Millimeter Wave Range," Journal of Infrared, Millimeter, and Terahertz Waves, vol. 31, no. 12, pp. 1503–1511, 2010.

[42] V. Chaudhary and R. Panwar, "FSS derived using a new equivalent circuit model backed Deep Neural Network," IEEE Antennas and Wireless Propagation Letters, vol. 20, no. 10, pp. 1963–1967, 2021.

[43] Maple series UV laser maple-355-5 - nanosecond lasers - huaray laser, http://en.huaraylaser.com/products_detail?product_id=47&;product_category=11 (accessed May 30, 2023).

[44] A. A. Serkov, H. V. Snelling, S. Heusing, and T. M. Amaral, “Laser sintering of gravure printed indium tin oxide films on polyethylene terephthalate for Flexible Electronics,” Scientific Reports, vol. 9, no. 1, 2019.

[45] C. Y. Leong et al., “Single Pulse laser removal of indium tin oxide film on glass and polyethylene terephthalate by nanosecond and femtosecond laser,” Nanotechnology Reviews, vol. 9, no. 1, pp. 1539–1549, 2020.

[46] A. Bhattacharjee, A. Bhawal, A. Karmakar, A. Saha, and D. Bhattacharya, “Vivaldi antennas: A historical review and current state of art,” International Journal of Microwave and Wireless Technologies, vol. 13, no. 8, pp. 833–850, 2020.

[47] C. A. Balanis, Antenna theory: Analysis and design. Chichester, West Sussex: Wiley Blackwell, 2016.

[48] D.-I. (F. H. C. Wolff, “Tapered Slot Antenna (Vivaldi- Antenna),” Radartutorial. [Online]. Available: https://www.radartutorial.eu/06.antennas/Tapered%20Slot%20Antenna.en.html. (accessed May 30, 2023).

[49] V. Naydenko and M. Kozachuk, “Vivaldi coplanar-antipodal antennas,” 2020 IEEE Ukrainian Microwave Week (UkrMW), 2020.

[50] J. D. S. Langley, P. S. Hall, and P. Newham, “Novel ultrawide-bandwidth Vivaldi antenna with low crosspolarisation,” Electronics Letters, vol. 29, no. 23, p. 2004, 1993.

[51] I. T. Nassar and T. M. Weller, “A novel method for improving antipodal Vivaldi Antenna Performance,” IEEE Transactions on Antennas and Propagation, vol. 63, no. 7, pp. 3321–3324, 2015.

[52] A. M. Abbosh, “Directive antenna for ULTRAWIDEBAND Medical Imaging Systems,” International Journal of Antennas and Propagation, vol. 2008, pp. 1–6, 2008.

[53] H. Özmen and M. B. Kurt, “Radar-based Microwave Breast Cancer Detection System with a high-performance ultrawide band Antipodal Vivaldi Antenna,” TURKISH JOURNAL OF ELECTRICAL ENGINEERING & COMPUTER SCIENCES, vol. 29, no. 5, pp.

[54] J. Bai, S. Shi, and D. W. Prather, “Modified compact antipodal Vivaldi antenna for 4–50-GHz UWB application,” IEEE Transactions on Microwave Theory and Techniques, vol. 59, no. 4, pp. 1051–1057, 2011.

[55] A. S. Turk and A. K. Keskin, “Partially dielectric-loaded ridged horn antenna design for Ultrawideband gain and Radiation Performance Enhancement,” IEEE Antennas and Wireless Propagation Letters, vol. 11, pp. 921–924, 2012.

[56] K. Hietpas, “Applications & Considerations for Double-Ridge Guide Horn Antennas,” Microwave Journal, https://www.microwavejournal.com/articles/35247-applications-considerations-for-double-ridge-guide-horn-antennas (accessed May 30, 2023).

[57] Y. C. Toy, P. Mahouti, F. Gunes, and M. A. Belen, “Design and manufactering of an X-band horn antenna using 3-D printing technology,” 2017 8th International Conference on Recent Advances in Space Technologies (RAST), 2017.

[58] Yohandri, R. A. Syafrindo, J. T. Sumantyo, C. E. Santosa, and A. Munir, “3D print X-band horn antenna for ground-based SAR application,” 2017 Progress In Electromagnetics Research Symposium - Spring (PIERS), 2017.

[59] I. J. Solomon, P. Sevvel, and J. Gunasekaran, “A review on the various processing parameters in FDM,” Materials Today: Proceedings, vol. 37, pp. 509–514, 2021.

[60] D. Popescu, A. Zapciu, C. Amza, F. Baciu, and R. Marinescu, “FDM process parameters influence over the mechanical properties of polymer specimens: A Review,” Polymer Testing, vol. 69, pp. 157–166, 2018.

[61] M. Spoerk, J. Gonzalez-Gutierrez, J. Sapkota, S. Schuschnigg, and C. Holzer, “Effect of the printing bed temperature on the adhesion of parts produced by fused filament fabrication,” Plastics, Rubber and Composites, vol. 47, no. 1, pp. 17–24, 2017.

[62] Tenigeer, N. Zhang, J.-H. Qiu, P.-Y. Zhang, and Y. Zhang, “Design of a novel broadband EMC Double Ridged Guide Horn Antenna,” Progress In Electromagnetics Research C, vol. 39, pp. 225–236, 2013.

[63] M. Puri, P. K. Mishra, S. S. Dhanik, and H. Khubchandani, “Design and simulation of double ridged horn antenna operating for UWB applications,” 2013 Annual IEEE India Conference (INDICON), 2013.

[64] F. Oktafiani, E. Y. Hamid, and A. Munir, “Wideband dual-polarized 3D printed quad-ridged horn antenna,” IEEE Access, vol. 10, pp. 8036–8048, 2022.

[65] L. Chen, C. Ong, C. Neo, and V. Varadan, Microwave Electronics: Measurement and Materials Characterization. John Wiley & Sons, 2005.

[66] “LRL/LRM Calibration Theory and Methodology,” Anritsu Application Note, https://dl.cdn-anritsu.com/en-us/test-measurement/files/Application-Notes/Application-Note/11410-00492C.pdf (accessed May 30, 2023).

[67] “Product documentation,” NI, https://www.ni.com/docs/en-US/bundle/ni-vna/page/vnahelp/calibration_trl.html (accessed May 30, 2023).

[68] A. M. Nicolson and G. F. Ross, “Measurement of the intrinsic properties of materials by time-domain techniques,” IEEE Transactions on Instrumentation and Measurement, vol. 19, no. 4, pp. 377–382, 1970.

[69] F. Costa, M. Borgese, M. Degiorgi, and A. Monorchio, "Electromagnetic characterisation of materials by using transmission/reflection (T/R) devices," Electronics, vol. 6, no. 4, p. 95, 2017.

[70] Keysight, "N1500A materials measurement suite," Keysight, https://www.keysight.com/us/en/product/N1500A/materials-measurement-suite.html (accessed May 30, 2023).

[71] P. G. Bartley and S. B. Begley, "A new technique for the determination of the complex permittivity and permeability of materials," 2010 IEEE Instrumentation & Measurement Technology Conference Proceedings, 2010.

[72] B. Riddle, J. Baker-Jarvis, and J. Krupka, "Complex permittivity measurements of common plastics over variable temperatures," IEEE Transactions on Microwave Theory and Techniques, vol. 51, no. 3, pp. 727–733, 2003.

[73] H. E. Bussey, D. Morris, and E. B. Zal'tsman, "International comparison of complex permittivity measurement at 9 GHz," IEEE Transactions on Instrumentation and Measurement, vol. 23, no. 3, pp. 235–239, 1974.

[74] J. Krupka, "Measurements of the complex permittivity of low loss polymers at frequency range from 5 GHz to 50 GHz," IEEE Microwave and Wireless Components Letters, vol. 26, no. 6, pp. 464–466, 2016.

[75] N. Gorshkov et al., "Dielectric properties of the polymer–matrix composites based on the system of co-modified potassium titanate–polytetrafluorethylene," Journal of Composite Materials, vol. 52, no. 1, pp. 135–144, 2017.

[76] F. Gonçalves, A. Pinto, R. Mesquita, E. Silva, and A. Brancaccio, "Free-space materials characterization by reflection and transmission measurements using frequency-by-frequency and multi-frequency algorithms," Electronics, vol. 7, no. 10, p. 260, 2018.

[77] "EccosorbTM" Laird Performance Materials, https://www.laird.com/products/microwave-absorbers/microwave-absorbing-foams/eccosorb-an (accessed May 30, 2023).